

MULTIPLE STELLAR POPULATIONS OF GLOBULAR CLUSTERS FROM HOMOGENEOUS Ca -CN PHOTOMETRY. II. M5 (NGC 5904) AND A NEW FILTER SYSTEM.¹

Jae-Woo Lee^{2,3}

ABSTRACT

Using our ingeniously designed new filter systems, we investigate the multiple stellar populations (MSPs) of the red giant branch (RGB) and the asymptotic giant branch (AGB) in the globular cluster (GC) M5. Our results are the following. (1) Our cn_{JWL} index accurately traces the nitrogen abundances in M5, while other color indices fail to do so. (2) We find bimodal CN distributions both in the RGB and the AGB sequences, with the number ratios between the CN-weak (CN-w) and the CN-strong (CN-s) of $n(\text{CN-w}):n(\text{CN-s}) = 29:71 (\pm 2)$ and $21:79 (\pm 7)$, respectively. (3) We also find the bimodal photometric $[N/Fe]$ distribution for M5 RGB stars. (4) Our $cn_{JWL}-[O/Fe]$ and $cn_{JWL}-[Na/Fe]$ relations show the clear discontinuities between the two RGB populations. (5) Although small, the RGB bump of the CN-s is slightly brighter, $\Delta V_{\text{bump}} = 0.07 \pm 0.04$ mag. If real, the difference in the helium abundance becomes $\Delta Y = 0.028 \pm 0.016$, in the sense that the CN-s is more helium enhanced. (6) Very similar radial but different spatial distributions with comparable center positions are found for the two RGB populations. The CN-s RGB and AGB stars are more elongated along the NW-SE direction. (7) The CN-s population shows a substantial net projected rotation, while that of the CN-w population is nil. (8) Our results confirm the deficiency of the CN-w AGB stars previously noted by others. We show that it is most likely due to the stochastic truncation in the outer part of the cluster. Finally, we discuss the formation scenario of M5.

Subject headings: globular clusters: individual (M5: NGC 5904) — Hertzsprung-Russell diagram — stars: abundances — stars: evolution

1. INTRODUCTION

During the last decade, a drastic paradigm shift on the true nature of the Galactic globular clusters (GCs) has emerged. Almost all GCs exhibit variations in lighter elemental abundances, for example bimodal CN distributions and Na-O anticorrelations (e.g., Smith 1987; Carretta et al. 2009). Understanding this ubiquitous nature of the multiple stellar populations (MSPs) in GCs is one of the outstanding quest in the near field cosmology (e.g., Lee et al. 2009a; Lee 2015; Piotto et al. 2015; Renzini et al. 2015).

The key feature of the MSPs in the peculiar GCs, like ω Cen and M22, is the discrete distributions in the heavy elemental abundances and these GCs are considered to be remnants of the dwarf galaxy related

¹Based on observations made with the Cerro Tololo Inter-American Observatory (CTIO) 1m telescope, which is operated by the SMARTS consortium.

²Department of Physics and Astronomy, Sejong University, 209 Neungdong-ro, Gwangjin-Gu, Seoul, 05006, Korea; jae-woolee@sejong.ac.kr, jaewoolee@sejong.edu

³Visiting Astronomer, CTIO, National Optical Astronomy Observatories (NOAO), operated by the Association of Universities for Research in Astronomy, Inc., under cooperative agreement with the National Science Foundation.

objects and accreted to the Milky Way later in time (Y.-W. Lee et al. 1999; Lee et al. 2009a; Lee 2015, 2016; Johnson & Pilachowski 2010; Marino et al. 2011b). On the other hand, the normal GCs exhibit the significant spread in the lighter elemental abundances, which is resulted from the proton capture process at high temperature, most likely engraved during the multiple phases of star formation history¹ (e.g., D’ercole et al. 2008; Carretta et al. 2009).

How normal GCs formed is still under debate. By and large, four potential candidates of the source of the proton capture process at high temperature and helium enhancement have been proposed, which are (i) asymptotic giant (AGB) stars (D’ercole et al. 2010); (ii) fast rotating massive stars (Decressin, Charbonnel, & Meynet 2007); (iii) interacting massive binaries (De Mink et al. 2007); and (iv) supermassive stars (Denissenkov & Hartwick 2014). Each candidate has pros and cons to explain the observational lines of evidence in GCs. In the context of the self-enrichment scenario for normal GCs, Renzini et al. (2015) proposed that the AGB pollution scenario would be favored. However, most of the proposed candidates cannot solve the so-called “mass-budget problem” with satisfaction (e.g., see Bastian & Lardo 2015). The GCs with MSPs formation scenario proposed by Bastian et al. (2013) can mitigate the mass-budget problem, but their model cannot explain the differences in the spatial distributions and kinematics between the MSPs in M5, as we will discuss later.

The ultra-violet photometry from the *Hubble Space Telescope* (*HST*) or the high-resolution spectroscopy using the *Very Large Telescopes* (*VLT*) have long been the most reliable passages into the realm of the high precision MSP study of the Galactic or extra-Galactic GC systems (e.g. Carretta et al. 2009; Piotto et al. 2015). The variations in the lighter elemental abundances, such as C, N and O, greatly affect the UV regime through OH, NH, CN and CH molecular bands. These molecular bands are often very strong and the variations of lighter elemental abundances can be detected even with the wide-band photometry. In this context, the photometric approach is still important for the sake of completeness (in particular in the central part of GCs where the spectroscopic method can not be applied) and easiness.² Therefore, studies of MSPs in GCs through photometry and spectroscopy are complementary.

It is very unfortunate that only a few groups of astronomers around the globe are permitted to access these prestigious instruments, such as the *HST* or the *VLT*, for over decades, which made the competition unfair. As a result of our decade long hard effort, we developed a new approach that small aperture telescopes empowered by ingeniously designed narrow-band filter systems can have a capability to measure not only the heavy but also the lighter elemental abundances of the RGB and AGB stars in GCs. Our novel approach is very straightforward and easy to apply, which can open a new era of prolific discoveries in the field of the MSPs in our Galaxy with mere 1-m or sub 1-m class telescopes. Also, our results presented here and in the future will complement the intrinsic weakness of the aforementioned instruments, such as the *HST* and the *VLT* (Lee 2010, 2015, 2016).

This is a part of the series of papers addressing the MSPs of Galactic GCs based on our homogeneous *Ca*-CN photometry. In our previous study (Lee et al. 2009a,b; Lee 2015), we extensively demonstrated that the so-called extended Strömgren photometry (Anthony-Twarog et al. 1991) can provide a very powerful means to study MSPs with heterogeneous metallicity. In our current study, we explore the CN abundances of the RGB and the AGB stars in M5, one of the first archetype of the GC with the CN inhomogeneity (Osborn 1971), using our new filter system, *JWL39*.

The outline of the paper is as follows. We describe the Sejong *Ca*-CN survey program, our newly

¹See Lee (2010) for the effect of the internal mixing in the RGB stars.

²See Lee (2016) for the non-trivial aspects of the LTE analysis of high-resolution spectroscopy of GC RGB stars.

devised filter system, *JWL39*, and new color index associated with it in Section 2. We show observations and data reduction of M5 in Section 3. Some very interesting results on the M5 RGB and AGB stars will be presented in Section 4. Finally, we address the summary and discussion in Section 5. In appendix, we show the artificial star experiments to examine the completeness of our photometry. We also show a new strategy for the ground-based observations by making use of the positional information from the *HST* photometry, which can significantly improve any of ground-based observations of the very crowded region.

2. A NEW CN FILTER SYSTEM: *JWL39*

Sejong *Ca*-CN (formerly, Sejong *Ca by*) survey program was launched in July, 2006. As an official major partner of the SMARTS consortium, we acquired the guaranteed access to the small telescopes operated at the CTIO since 2006. The summary of our survey program can be found in Lee (2015).

Our survey program is consisted of three phases. The Phase I was from July, 2006 to November, 2010 (see Lee et al. 2009a,b). During this period, we used Strömgren *wby* and *Ca* filters provided by the CTIO. The CN band at λ 3883 Å is often very strong in the RGB stars and the CTIO *Ca* filter was originally designed to avoid the CN band contamination. However, it was suspected that the CTIO *Ca* filter had undergone degradation due to aging effect and the original transmission function had been altered to the shorter wavelength. As a result, the CTIO *Ca* filter is suspected to suffer from the CN band contamination. Note that we do not use the *Ca* photometry from the Phase I for our current work presented here.

Since March 2011 (Phase II), we used our own Strömgren *by* and new *Ca* filters, all of which were manufactured by Asahi Spectra, Japan. Our new *Ca* filter was carefully designed by the author of the paper to have very similar filter bandwidth and pivot wavelength as those of F395N filter in the Wide-Field Camera 3 (WFC3) onboard the *HST*. In Figure 1, we show a comparison of filter transmission functions between that in Anthony-Twarog et al. (1991) and that of our new *Ca* filter measured with collimated beam by the manufacturer of the filter. Both filter have similar full-width at the half maximums (FWHMs), approximately 90 Å but our new *Ca* filter has a more uniform and high transmission across the passband, dropping more rapidly at both edges. As shown in the figure, the CN band at λ 3883 Å lies on the lower tail of the *Ca* filter by Anthony-Twarog et al. (1991) while our new *Ca* filter is designed to be completely free from the CN band contamination.

In the Phase III started in April 2013, we added a new filter system also designed by the author of the paper, *JWL39*, which allows us to measure the CN band at λ 3883 Å in combination with our new *Ca* filter. Note that our *JWL39* filter is somewhat similar to the DDO38 filter (McClure & van den Bergh 1968), but our filter has the slightly different bandwidth and the pivot wavelength. We show the transmission function of our *JWL39* filter in Figure 1.

In Table 1, we show the pivot wavelengths, bandwidths and spectral resolutions of various filter system used in the ultra-violet (UV) and in the blue part of the visible light. Note that the *HST* filter systems shown in the table are for the so-called “*magic-trio*”, a combination of *HST* WFC3/UVIS F275W, F336W and F438W filters (Milone et al. 2013). As Piotto et al. (2015) nicely demonstrated, the *HST* magic-trio is known to distinguish the multiple stellar populations in GCs. However, the interpretation of the magic-trio can be somewhat complicated because it measures OH, NH, CN, CH and Mg (through Mg II h & k) at the same time (see Figure 2). Even worse is that the CN molecular bands are expected to show a positive luminosity effect while the OH, NH and CH bands are expected to show a negative luminosity effects due to the lower dissociation energies of the hydrate molecules (for example, see Gray & Corbally 2009). The UV

filters with very wide bandwidths ($\Delta\lambda > 50$ nm), such as the filters used in the *HST* magic-trio, Johnson *U*, *SDSS u* and Washington *C*, has some disadvantages, too. These filters contain numerous very strong lines other than CNO and small changes in the elemental abundances or in the stellar parameters can affect the absorption strength and the continuum and, hence, the photometric index using such wide band filters. It is important to note that the NH band lies near the boundaries of the steeply decreasing transmission functions of the Johnson *U*, Washington *C*³, *SDSS u* and Strömgren *u* filters, where the degree of the atmospheric extinction also increases very rapidly. Therefore these ill-matched combinations of the transmission of these filters and the atmospheric extinction make their photometric systems less sensitive to the NH abundances, as we will show later. In sharp contrast, our cn_{JWL} index ($= JWL39 - C_{a_{new}}$) is intended to measure the CN λ 3883 Å band absorption strength only and the atmospheric extinction does not vary significantly in the *JWL39* passband. We will show later that our cn_{JWL} index is as good as $S(3839)$ or $\delta S(3839)$ from low resolution spectroscopy and capable of distinguishing MSPs in GCs with great satisfaction.

3. OBSERVATIONS AND DATA REDUCTION

Observations for M5 were made in 21 nights, 12 of which were photometric, in 7 runs from May 2007 to May 2014 using the CTIO 1.0m telescope. The CTIO 1.0m telescope was equipped with a STA $4k \times 4k$ CCD camera, providing a plate scale of $0''.289 \text{ pixel}^{-1}$ and a field of view (FOV) of about $20' \times 20'$. During the whole seasons, the mean seeing from our M5 science frames is $1''.53 \pm 0''.27$. In Table 2, we show the total integration times for M5.

The detailed procedures for the raw data handling were described in our previous works (Lee et al. 2014; Lee 2015; Lee & Pogge 2016). The photometry of the cluster and photometric standard frames were analyzed using DAOPHOTII, DAOGROW, ALLSTAR and ALLFRAME, and COLLECT-CCDAVE-NEWTRIAL packages (Stetson 1987, 1994, 1995). In appendix B, we present a new strategy for the ground-based observations to make use of the positional information from the *HST* photometry by Anderson et al. (2008), which greatly improve the detection rate in the central part of the cluster ($r \lesssim r_h$).⁴ The total number of stars measured in our M5 field from our ALLFRAME run was more than 60,000.

Astrometric solutions for individual stars in our field were derived using the data extracted from the Naval Observatory Merged Astrometric Dataset (NOMAD, Zacharias et al. 2004) and the IRAF IMCOORS package. Then the astrometric solution was applied to calculate the equatorial coordinates for all stars measured in our science frames.

4. RESULTS

4.1. Color-magnitude diagrams

Figure 3 shows the color-magnitude diagrams (CMDs) of bright stars in the M5 field. We used photometric results from our new filters for $(b - y)$, hk and cn_{JWL} which were taken after 2011, while those from the CTIO filters for $m1$, cy and $(u - y)$, which were taken before 2011. As can be seen in the figure,

³See Cummings et al. (2014) for the usage of the Washington *C* filter for the MSPs in NGC 1851.

⁴The half-light radius of M5 is $r_h \approx 106''$ (Harris 1996).

$(b - y)$ and hk CMDs show rather narrow single RGB sequences without any significant spread, confirming previous results that M5 is a mono-metallic cluster (e.g. Ivans et al. 2001; Carretta et al. 2009). On the other hand, $m1$, cy and cn_{JWL} CMDs exhibit very broad or even discrete double RGB sequences, indicative of the spread in the lighter elemental abundances, more specifically, a significant spread or a bimodal distribution of the nitrogen abundance because these color indices contain either NH or CN, or both, as already shown in Figure 2. In particular, the clear split in the RGB sequence in the cn_{JWL} versus V CMD is evident. We will show later that M5 most likely has a bimodal nitrogen abundance distribution, which is consistent with our cn_{JWL} index showing the discrete double RGB sequences. What makes our cn_{JWL} index great is that it is a photometric index so that one can measure very accurate CN λ 3883 Å band absorption strengths of cool RGB and AGB stars in the very crowded region. On the other hand, the distinction between the different populations is somewhat ambiguous in cy and $m1$ indices in Figure 3. The results from these two color indices should be used to detect the spread in the lighter elemental abundances only and not be used for the detailed chemical tagging.

Based on our cn_{JWL} versus V CMD, we derive the number ratio between the two groups of stars, the CN-w and the CN-s (see below for the definitions). We carefully chose RGB membership stars using our multi-color photometry and we show our results in Figure 4. As elaborately shown in our previous work (Lee 2015), our method is very effective to remove the off-cluster field stars even for heavily field star contaminated GCs like M22. Since M5 is located in a rather high Galactic latitude, $b = 46^\circ.8$, the field star contamination is expected to be not severe in our results. Assuming a bimodal cn_{JWL} distribution, we applied the expectation maximization (EM) algorithm for the two-component Gaussian mixture model to distinguish the different RGB populations. In an iterative manner, we calculated the probability of individual stars for being the CN-w and the CN-s populations. Stars with $P(\text{CN-w}|x_i) \geq 0.5$ from the EM estimator correspond to the CN-w population, where x_i denotes the individual RGB stars, while those with $P(\text{CN-s}|x_i) > 0.5$ correspond to the CN-s population. Through this process, we obtained the number ratio between the two populations, $n(\text{CN-w}):n(\text{CN-s}) = 29:71 (\pm 2)$.

4.2. Red giant stars

4.2.1. A comparison with Briley et al. (1992)

Briley et al. (1992) performed a spectroscopic study of M5 RGB star and they derived the nitrogen abundances of RGB stars. As already shown in Figure 3, the $(b - y)$ and hk CMDs show narrow single RGB sequences and any significant differences in the positions of the CN-w and the CN-s RGB stars defined by Briley et al. (1992) can not be seen. On the other hand, correlations between the nitrogen abundance and color indices can be found in $m1$, cy and cn_{JWL} CMDs, although correlations involved with $m1$ and cy indices do not look as good as that with cn_{JWL} .

First, we examined the correlations between the CN λ 3883 Å absorption strengths by Briley et al. (1992), $S(3839)$, and the color indices that we measured. In Figure 5(a)–(c), we show plots of $S(3839)$ versus each color index, and the goodness of the fits in Table 3. Note that the p -value of the fit for the $m1$ versus $S(3839)$ is as good as that for the cn_{JWL} versus $S(3839)$, but the figure clearly shows that the $m1$ index is not capable of discriminating the two different populations. On the $m1$ versus $S(3839)$ or $\delta S(3839)$ planes, the CN-w and the CN-s populations by Briley et al. (1992) are superposed each other. In panel (a), the distributions of the bright and the faint RGB stars are clearly divided around the fitted line, indicating that the differences in the temperature and the surface gravity may affect the $S(3839)$ values at different V

magnitudes. In order to correct these effects, we derive the CN excess, $\delta S(3839)$, which is the distance in $S(3839)$ from the lower envelope of the distribution of RGB stars in the V magnitude versus $S(3839)$,

$$\delta S = S(3839) - (1.287 - 0.088 \times V). \quad (1)$$

Note that Briley et al. (1992) did not provide $\delta S(3839)$. Our results are shown in panels (d)–(f). As shown, using $\delta S(3839)$ greatly improves the linear fit for our cn_{JWL} index, with the correlation coefficient of 0.941 and the p -value of 0.000. On the other hand, both the cy and the $m1$ indices do not accurately trace the CN excess.

In Figures 3 and 4, the cy and the $m1$ indices show considerable curvatures in the RGB magnitude level of our interest, indicative of the presence of the temperature and surface gravity effects upon these indices. In order to correct these effects, we derived the excess in the cy and $m1$ indices, δcy and $\delta m1$, which are the distances from the outer envelopes of RGB distributions in each index at fixed V magnitude, finding,

$$\delta cy = cy - (-4.030 - 0.480V - 0.015V^2) \quad (2)$$

and

$$\delta m1 = m1 - (3.050 - 0.329V + 0.009V^2). \quad (3)$$

Again, as shown in Figure 5(g–j), neither δcy nor $\delta m1$ appear to mitigate the discrepancy, suggesting that both indices are not good CN tracers.

Next, we examine the correlations between the nitrogen abundances and color indices. In Figure 6, we show least square fits between the nitrogen abundance by Briley et al. (1992) and individual color indices. Since the visual magnitude of the RGB stars studied by Briley et al. (1992) has a gap, we divided the sample into two groups, the bright ($V \leq 14.5$ mag) and the faint ($V \geq 15.5$ mag) RGB groups. We derived the linear correlations to the data and we show our results in Table 4. The correlations between the nitrogen abundances and the cn_{JWL} index are excellent for both magnitude bins, with consistent slopes and zero points. The correlations between the nitrogen abundances and the cy and $m1$ indices are also excellent for the bright RGB stars. However, those for the faint RGB stars are very poor. Also importantly the least square fits for both magnitude bins are significantly different for $m1$ and cy indices, which make the both indices difficult to be good photometric indicators for nitrogen abundances.

We derive the photometric nitrogen abundance for individual RGB stars based on our linear correlations. We performed a Hartigan’s dip test to see if the nitrogen abundance distribution of M5 RGB stars by Briley et al. (1992) is unimodal. We obtained $D = 0.061$ and p -value = 0.870, suggesting that the nitrogen abundance distribution of the M5 RGB stars is non-unimodal. Therefore, assuming a bimodal distribution of the nitrogen abundance for M5, we applied the EM algorithm for the two-component Gaussian mixture distribution model to calculate the contributions from two populations. In an iterative manner, we derive the probability of individual RGB stars for being the CN-w and the CN-s populations and we show our result in Figure 7(a), with the number ratio between the CN-w and the CN-s populations of $n(\text{CN-w}):n(\text{CN-s}) = 28:72 (\pm 20)$.

Using the least square fits given in Table 4, we calculate the photometric nitrogen abundances of the RGB stars with $-2 \leq V - V_{\text{HB}} \leq 2$ mag. The photometric nitrogen abundance from our cn_{JWL} index provides a bimodal distribution as shown in Figure 7(b). The number ratio of the two populations based on the photometric nitrogen abundance from the cn_{JWL} index is $n(\text{CN-w}):n(\text{CN-s}) = 29:71 (\pm 2)$, in excellent agreement with the spectroscopic nitrogen abundance distribution by Briley et al. (1992) and that from our cn_{JWL} index. Our results strongly support that our cn_{JWL} index is truly a measure of the CN absorption

strength at $\lambda 3883 \text{ \AA}$, and furthermore the nitrogen abundance. On the other hand, the photometric nitrogen abundances from the $m1$ and cy indices shown in Figure 7(c-d) do not agree with the nitrogen abundance measurements by Briley et al. (1992), showing a conspicuous single peak with a rather long tail.

We conclude that our cn_{JWL} index traces the nitrogen abundance of RGB stars in M5, while the $m1$ and the cy indices can provide some limited information on the spread in the nitrogen abundances but fail to provide detailed substructures in the nitrogen abundance distribution.

4.2.2. A comparison with Smith, Modi, & Harmen (2013)

In Figure 8(a)-(b), we show the $(b - y)$ and the cn_{JWL} CMDs for M5 RGB and AGB stars used by Smith, Modi, & Harmen (2013), who compiled the $\lambda 3883 \text{ \AA}$ CN band strengths for the M5 RGB and AGB stars from the literature. As discussed earlier, there exists no difference between the CN-w and CN-s populations in the $(b - y)$ versus V CMD, while a clear split between the two populations, including the AGB stars, in the cn_{JWL} versus V CMD can be seen. We will discuss more about the AGB stars in §4.3.

It should be emphasized that our cn_{JWL} index do not show any gradient against the V magnitude in the region of our interest ($-2 \leq V - V_{\text{HB}} \leq 2 \text{ mag}$) for M5, which suggests that no temperature and surface gravity corrections are required for our cn_{JWL} index. We compare our cn_{JWL} index with the $S(3839)$ or the $\delta S(3839)$ measurements by Smith, Modi, & Harmen (2013) and we show our results in Figure 8(c)-(d) and Table 5. It can be clearly seen that our cn_{JWL} index correlates nicely with both $S(3839)$ and $\delta S(3839)$, indicating again that the cn_{JWL} index is a measure of the CN band strength at $\lambda 3883 \text{ \AA}$.

It is interesting to note that using the CN excess, $\delta S(3839)$, does not improve the correlations as we showed in Figure 5. It is suspected that it may be due to the heterogeneous nature of the sample stars used by Smith, Modi, & Harmen (2013).

4.2.3. A comparison with Carretta et al. (2009)

In Figure 9(a), we show the Na-O anticorrelation of M5 RGB stars studied by Carretta et al. (2009), where one can find M5 has an extended and well defined Na-O anticorrelation (e.g., see also, Ivans et al. 2001). In Figure 9(b), we show the cn_{JWL} versus V CMD of the RGB stars studied by Carretta et al. (2009), where the distinct double RGB sequences can be clearly seen. We show the histograms for the CN-w and the CN-s populations in Figure 9(c) and we obtain the number ratio of $n(\text{CN-w}):n(\text{CN-s}) = 25:75 (\pm 5)$ from the EM estimator, which is marginally in agreement with our results shown previously. Note that this number ratio does not represent the complete RGB number ratio of M5 because the sample RGB stars chosen by Carretta et al. (2009) are restricted to those adequate for the spectroscopic observations in the outer part of the cluster. In Figure 9(d)-(i), we show the $[\text{O}/\text{Fe}]$ and the $[\text{Na}/\text{Fe}]$ distributions for each population, where one can find that our cn_{JWL} index can nicely distinguish the primordial⁵ and other (i.e. the intermediate and the extreme) populations. As shown, the CN-w population from our cn_{JWL} index has higher oxygen and lower sodium abundances while the CN-s population has lower oxygen and higher sodium abundances (see also Figure 9 of Ivans et al. 2001). Of particular interest is the two separate $cn_{\text{JWL}}-[\text{O}/\text{Fe}]$ and the $cn_{\text{JWL}}-[\text{Na}/\text{Fe}]$ relations for both populations, i.e., the two separate $[\text{N}/\text{Fe}]-[\text{O}/\text{Fe}]$ and the $[\text{N}/\text{Fe}]-[\text{Na}/\text{Fe}]$

⁵The definition of the primordial population by Carretta et al. (2009) is the group of stars with $[\text{Na}/\text{Fe}] \leq 0.1 \text{ dex}$.

relations. In Figure 9(f), the [O/Fe] abundance of the CN-w RGB stars appear to increase (or, perhaps remains flat) against the cn_{JWL} index and then the [O/Fe] abundance of the CN-s RGB stars decreases with the cn_{JWL} index. In the plot, we also show the linear fits for each population. Smith, Modi, & Harmen (2013) also suspected non-continuous relations between their $\delta S(3839)$ measurements and either [O/Fe] or [Na/Fe]. However, due to their small sample size, their conclusion was somewhat provisional. We note that the same trend can also be seen in NGC 6752 (see Figure 9 of Yong et al. 2008), which will be discussed in our future work (Lee 2017a, in preparation).

It is also very interesting to note that the spread in the [O/Fe] abundance of the CN-s population, $\sigma[\text{O/Fe}] \approx 0.27$ dex, is very large compared to that of the CN-w population, $\sigma[\text{O/Fe}] \approx 0.09$ dex, while the spreads in the [Na/Fe] abundance for both populations are compatible, $\sigma[\text{Na/Fe}] \approx 0.15$ dex. In the context of the chemical evolution of GC stars, however, what really matter would be the total number of atomic species. We define the standard deviation of the numbers of the atom in GC RGB stars,

$$\sigma[\text{X}] = \log[\sigma\langle 10^{\lfloor \log(\text{X/H}) + 12 \rfloor} \rangle]. \quad (4)$$

Despite the factor of 2 difference in the mean oxygen abundances between the two populations, $\langle \log(\text{O/H}) + 12 \rangle = 7.78$ for the CN-w stars and 7.47 for the CN-s stars, we obtained the very similar values for the standard deviations of the numbers of the oxygen atom, $\sigma[\text{O}] = 7.11$ for the CN-w stars and 7.18 for the CN-s stars. On the other hand, the standard deviations of the numbers of the sodium atom are quite different between the two populations, $\sigma[\text{Na}] = 4.43$ for the CN-w stars while 4.86 for the CN-s stars.

Finally, we show CMDs of spectroscopic target RGB stars of Carretta et al. (2009) in Figure 10. As we mentioned before, the $m1$ and cy indices are capable of detecting non-uniform lighter elemental abundances. However, the level of confusion is severe so that both indices cannot clearly separate different populations as we pointed out previously. Only the cn_{JWL} index can fully separate the primordial population from the others, where no clear distinction between the intermediate and the extreme populations can be seen from the photometric point of view as shown in the figure. This is also the case for the $\delta S(3839)$, as noted by Smith, Modi, & Harmen (2013). In the figure, the superpositions of the primordial and the intermediate populations can be seen in the cn_{JWL} index. It is most likely due to the arbitrary definition of the boundary between the two populations set by Carretta et al. (2009) in the continuous distribution of the RGB stars on the [O/Fe] versus [Na/Fe] plane.

4.2.4. A comparison with Lardo et al. (2011)

Using the *SDSS* archive data, Lardo et al. (2011) studied MSPs in GCs, including M5. Based on their newly devised normalized color spread, Δ'_{color} , they claimed that the radial distributions of the the UV-blue (i.e., the FG of the stars) and the the UV-red stars (the SG of stars) in M5 are distinctively different, in the sense that the UV-red stars are more centrally concentrated.

It is thought that using the *SDSS* photometry in the study of the MSPs in GCs has some potential problems. As already shown in Figure 2, the *SDSS* u filter contains the NH and the CN bands, where the atmospheric extinction becomes stronger at shorter wavelength. As a consequence, it is suspected that the *SDSS* u magnitude or color indices involved with it become less sensitive to changes in the nitrogen abundance. Also importantly, the *SDSS* g filter is very broad ($\Delta\lambda \approx 140$ nm) and it contains many strong molecular bands, such as CN, CH and MgH. Therefore, the color index composed of the *SDSS* u and g filters may behave in a complicated way against the changes in the light elemental abundances. Here we compare our photometry to that from the *SDSS* to see if both photometric systems provide consistent results.

In Figure 11, we show a comparison of our cn_{JWL} and Δ'_{u-g} by Lardo et al. (2011). Our cn_{JWL} versus V CMD nicely shows double RGB sequences with the number ratio of $n(\text{CN-w}):n(\text{CN-s}) = 27:73 (\pm 3)$. Again, this number ratio is not a complete one, but the one restricted by the sample RGB stars used by Lardo et al. (2011). On the other hand, the distributions of stars from both populations are continuously superposed on the Δ'_{u-g} versus g CMD, showing no clear separation between the two RGB sequences. The color indices using the *SDSS* u filter appears to suffer from confusion in discriminating the MSPs in GCs, as we already demonstrated for the cy and $m1$ indices. In particular, note that the CN-w RGB stars take larger range in the Δ'_{u-g} index than the CN-s stars. As shown, the histogram for the Δ'_{u-g} index exhibits a rather long asymmetric tail. We performed a Hartigan's dip test to see if the bimodality of the RGB stars along the Δ'_{u-g} is real, and this test suggests a bimodal Δ'_{u-g} distribution. Therefore, we applied an EM estimator, finding $n(\text{UV-blue}_{\text{JWL}}):n(\text{UV-red}_{\text{JWL}})^6 = 18:82 (\pm 3)$, which is significantly different from that of our photometry. Also note the very large standard deviation for the $\text{UV-blue}_{\text{JWL}}$ population compared to that of the $\text{UV-red}_{\text{JWL}}$. Originally, Lardo et al. (2011) classified stars with $\Delta'_{u-g} < -2$ as the UV-blue and stars with $\Delta'_{u-g} \geq -2$ as the UV-red . Using their classification scheme, we obtained the number ratio of $n(\text{UV-blue}):n(\text{UV-red}) = 32:68 (\pm 3)$, apparently consistent with that of our photometry. However, both the UV-blue and the UV-red groups defined by Lardo et al. (2011) contain mixed populations, i.e., the CN-w and the CN-s. It is thought that their boundary between the two populations is somewhat arbitrary in the continuous distribution of the two mixed populations in the Δ'_{u-g} distribution and there is no astrophysical basis for it. Since Lardo et al. (2011) used the RGB stars with $r \gtrsim 1'$ as shown in Figure 11, the confusion of the populations in the *SDSS* photometric system can not be attributed to the crowding effect. It is a rather intrinsic drawback of the *SDSS* u filter, in addition to its very broad passband in the UV ; Simply an ill-matched combination of the filter transmission and the atmospheric extinction is not adequate to study the NH band absorption features to characterize the MSPs in GCs. We suggest that, for example, the Δ'_{u-g} should be used only for detection of the light elemental abundance variations, but not be used for the detailed chemical tagging of individual stars, same as the cy and the $m1$ indices as we discussed above.

4.2.5. A comparison with Piotto et al. (2015)

We make a comparison of our photometry with the *HST* UV photometry by Piotto et al. (2015). Note that the *HST* photometry is available only for the central part of the cluster ($r \lesssim 1'$). In spite of our new data reduction strategy (see Appendix B), our ground-based photometry may suffer from incompleteness due to the very dense environment of the cluster's center. This is an unavoidable weakness of any ground-based observations, however, we emphasize that this should not affect our results shown here.

From our cn_{JWL} versus V CMD for common stars, we obtained $n(\text{CN-w}):n(\text{CN-s}) = 30:70 (\pm 3)$, consistent with our previous results, and we show our results in Figure 12. On the other hand, the RGB number ratio based on the $\Delta_{\text{C F275W,F336W,F438W}}$ is $26:74 (\pm 4)$, still marginally consistent with that from our photometry. It should be emphasized that there exists a good correlation between our cn_{JWL} and the $\Delta_{\text{C F275W,F336W,F438W}}$. As shown in Figure 2, the *HST* F336W filter covers the whole NH band features and, furthermore unlike other ground-based observations, it is free from the atmospheric extinction, leading the $\Delta_{\text{C F275W,F336W,F438W}}$ to be sensitive to the NH abundances. Therefore, it is not a surprise that there is a tight correlation between our cn_{JWL} and the $\Delta_{\text{C F275W,F336W,F438W}}$, which is a photometric analogue of

⁶ Note that the $\text{UV-blue}_{\text{JWL}}$ and the $\text{UV-red}_{\text{JWL}}$ denote the two groups of RGB stars based on our EM estimator and they are not the UV-blue and the UV-red populations originally defined by Lardo et al. (2011).

the NH-CN positive correlation seen in GC RGB stars, although some confusion in the *HST* photometry can be seen in the figure. We note that Milone et al. (2017) presented the fraction of the FG stars in M5, finding 0.235 ± 0.013 (see their Table 2), and their value is significantly different from our value. It is thought that the difference in the FG frequency arose from the different definitions of MSPs in both studies. It is also important to note that their FOV for M5 covers only the radial distance of $0.9r_h$ from the cluster’s center, although M5 does not show any radial gradient in the population ratio.

We conclude that our cn_{JWL} index can outperform the *HST* $\Delta_{\text{C F275W,F336W,F438W}}$. Incompleteness and, perhaps, inaccuracy in any ground-based photometry for the central part of the very dense GCs is unavoidable. However, a definite advantage of our observations is a very large FOV compared to the *HST* observations. As mentioned before, the FOV of our instrument setup can cover more than 55 times larger area than the *HST* can. The large FOV is one of the critical requirements to delineate the complete picture of the formation of the MSPs in GCs. We emphasize that our photometry presented here is adequate to such requirements.

4.2.6. RGB bump magnitude: V_{bump}

The helium abundance of GCs is very difficult to measure due to the absence of helium absorption lines in the visible spectra of the cool RGB stars. Instead, one can rely on the indirect methods to estimate the helium abundance using the helium sensitive features during the evolution of the low mass stars, which include the RGB bump luminosity (e.g. Cassisi & Salaris 2013) and the number ratio of the horizontal branch (HB) to RGB stars (Buzzoni et al. 1983).

We compare the RGB bump magnitudes of each populations in order to explore the difference in the helium abundance in a relative sense. In Table 6, we present our measurements for RGB bump V magnitudes for each population. We obtained $V_{\text{bump}} = 15.038 \pm 0.030$ and 14.970 ± 0.030 for the *Ca-w* and the *Ca-s* RGB stars, respectively. In particular, the V_{bump} of the *Ca-s* population, which is the major component of the cluster, is in good agreement with that of Sandquist et al. (1996), who obtained 14.964 ± 0.007 . In the central part of M5 ($r \leq 1'$), the V_{bump} magnitudes for both populations are slightly brighter than those in the outer part of the cluster ($r > 1'$). However, the differences are no larger than 0.01 ± 0.04 mag, exhibiting no effective radial fluctuations in the V_{bump} magnitude (see also Appendix B). We show CMDs around the RGB bump for both populations in the top panels of Figure 13 and the differential and cumulative luminosity functions in the lower panels. Although small, our measurements suggest that the visual magnitude of RGB bump of the CN-s population is slightly brighter by $\Delta V_{\text{bump}} = 0.07 \pm 0.04$ mag than that of the CN-w population.

It is well known that at a given age the RGB bump becomes fainter with increasing metallicity and with decreasing helium abundance, due to changes in the envelope radiative opacity (e.g., see Cassisi & Salaris 2013). As we have shown in our previous study (Lee 2015), one can quantitatively estimate the effect of metallicity and the helium abundance on the RGB bump luminosity. In their Table 2, Bjork & Chaboyer (2006) presented how the absolute V magnitude of the RGB bump depends on both age and metallicity and we derived $\Delta M_{V,\text{bump}}/\Delta[\text{Fe}/\text{H}] \approx 0.93$ mag/dex for 13 Gyr from their data. It is very unlikely,⁷ however, the age difference of about 2 Gyr between the two populations can result in the V_{bump} magnitude of the

⁷See Figures 26 and 27 for the precision *HST ACS* photometry of M5 (Anderson et al. 2008), where no discernible sign of age spread can be seen in its main-sequence (MS) turn-off point.

younger population to be 0.08 mag brighter.

The effect of helium abundance on the RGB bump can be found in Valcarce, Catelan, & Sweigart (2012). From their Figure 9, we obtained $\Delta m_{\text{bol}} \approx 2.5 \times \Delta Y$ for the isochrones with $Z = 1.6 \times 10^{-3}$ and 12.5 Gyr. The previous spectroscopic studies by others (Ivans et al. 2001; Carretta et al. 2009) and our current photometric study of the cluster suggest that there is no metallicity spread in M5. Assuming no age difference, there should be no metallicity effect on the V_{bump} magnitude and the bolometric corrections should be the same for both populations. Hence, the difference in the RGB bump magnitude of 0.07 ± 0.04 mag can be translated into the difference in the helium abundance of $\Delta Y = 0.028 \pm 0.016$, in the sense that the CN-s RGB stars are slightly more helium enhanced.

We conclude that the two RGB populations defined by our cn_{JWL} index exhibit the different chemical compositions: the CN-w population has high [O/Fe] and low [N/Fe], [Na/Fe] abundances, while the CN-s population has low [O/Fe] and high [N/Fe], [Na/Fe] abundances with the sign of a helium enhancement. In the context of the self enrichment scenario, therefore, our CN-w population is equivalent to the first generation (FG) of the stars, while the CN-s population is the second generation (SG) of the stars.

4.2.7. Centers

As a first step to compare the structural differences between the two populations, we measured the centers of each population using three different methods; the arithmetic mean, the half-sphere and the pie-wedge methods (see also, Lee 2015).

Using the coordinate of the center of the cluster measured by Goldsbury et al. (2010) as an initial value we chose RGB stars in each population within $3r_h$ ($\approx 320''$) from the center of the cluster and we calculated the mean values for each group.

We obtained the offset values with respect to the coordinate of the cluster's center by Goldsbury et al., $(\Delta\alpha, \Delta\delta) = (8''.2, 5''.2)$ for the CN-w population and $(-2''.5, 3''.2)$ for the CN-s population, resulted in an angular separation of about $11''$ between the centers of both populations. Note that the core radius of M5 is about $26''$ (Harris 1996), and the angular separation between the centers of the two populations is considered to be relatively small.

Similar to the simple mean calculation, we use the coordinate of the cluster by Goldsbury et al. as an initial value, we chose RGB stars in each population within $3r_h$ from the center of the cluster. Then we divided the sphere into two halves by assuming the radial symmetry in the distribution of RGB stars in M5. We compared the number of RGB stars between the two halves by rotating the position angle by 10 degree at a fixed coordinate of the center and we obtained the differences in the number of RGB stars between both halves. We repeated this calculation with varying coordinates of the center and we derived the coordinates of the centers of each population with the minimum difference in the number of RGB stars between the two halves. We obtained $(9''.5, 0''.6)$ for the CN-w population and $(0''.6, 1''.5)$ for the CN-s population, slightly different from those from the simple mean method. The angular separation between the two populations is about $9''$ and, again, it is relatively small compared with the core radius of the cluster.

Finally, we applied the pie-wedge method. We divided the sphere of a radius of $3r_h$ into 12 different slices. Then we compared the number of stars in the opposing distribution. We repeated this calculation with varying coordinates of the center and calculated the center of each population with the minimum differences. We obtained $(6''.5, 0''.5)$ for the CN-w population and $(-4''.2, 1''.3)$ for the CN-s population. Again, the

angular separation between the two populations is about $11''$ and it is still relatively small compared with the core or the half-light radii of the cluster.

We summarize our results in Table 7. We conclude that the coordinates of the centers of each population from bright RGB stars can be slightly different. However the differences in the coordinates of the center from various methods do not appear to be substantially large to claim that the centers of the two RGB populations are distinctively different.

4.2.8. Radial distributions

The radial distribution of the MSPs in GCs can provide crucial information on the GC formation and early chemical enrichment history, although the time scale required to homogenize the radial distributions of the MSPs is not clear (e.g., see Lee 2015).

First, we examined the radial distributions of RGB stars by Carretta et al. (2009). In Figure 14(a), we show the radial distributions of the primordial, the intermediate and the extreme populations. It can be clearly seen that the primordial population is the most centrally concentrated, while the extreme population is the least centrally concentrated. As discussed earlier, because there is no difference between the intermediate and the extreme populations from the photometric point of view, we combine the intermediate and the extreme populations together. We show a comparison of their distribution with that of the primordial population in Figure 14(b). Not surprisingly, the primordial population does look to be more centrally concentrated than the others, however, it may be due to the small number of sample in the spectroscopic study by Carretta et al. (2009). We performed a Kolmogorov-Smirnov (K-S) test and we obtained the significance level for the null hypothesis that the both distributions are drawn from the same distribution, $p = 0.329$, with a K-S discrepancy of 0.196, indicating that they are likely drawn from identical parent distributions. We also calculate the fraction of the primordial population, $n(P)/n(P+I+E) = 0.291 \pm 0.016$, and the fraction of the intermediate and the extreme populations, $n(I+E)/n(P+I+E) = 0.709 \pm 0.095$, consistent with our results based on the cn_{JWL} index.

Next, we examine the radial distribution of the CN-w and the CN-s populations from our cn_{JWL} index and we show our result in Figure 14(c), where the radial distributions of both populations look very similar. Our K-S test shows the significance level for the null hypothesis that the both distributions are drawn from the same distribution, $p = 0.300$, with a K-S discrepancy of 0.057, suggesting that the radial distributions of the CN-w and the CN-s populations are likely drawn from the identical parent distribution.

Finally, we note that the relative fractions of the CN-w and the CN-s RGB populations do not appear to vary against the radial distance from the center, albeit the radial distribution of the CN-w RGB population show some mild fluctuations due to the small number statistics in Figure 14. In Figure 15, we show the moving average from the adjacent 25 points for the cn_{JWL} index of the all RGB stars with $-2 \leq V - V_{HB} \leq 2$ mag against the radial distance from the center. The moving average shows some small scale local fluctuations but does not show any large scale gradient in the figure, i.e., no radial CN gradient in M5 (e.g., see Chun & Freeman 1979, for the radial CN variation in NGC 104). It is thought that the flat number ratio against the radial distance between the two populations up to more than $5r_h$ may suggest that M5 is already in the stage of complete mixing (e.g., see Vesperini et al. 2013).

4.2.9. Surface brightness profiles

The surface brightness profile (SBP) also provides a useful means to compare the structural property and we explore the SBPs of M5 RGB stars in each population. In Figure 16, we show the SBPs of the bright RGB stars ($-2 \leq V - V_{\text{HB}} \leq 2$ mag) in the CN-w and the CN-s populations. Also shown is the Chebyshev polynomial fit of the M5's SBP by Trager, King, & Djorgovski (1995). Our SBP measurements for both populations are in excellent agreement with that of Trager, King, & Djorgovski (1995) up to $10'$ (more than $5r_h$) from the center. Our SBP measurements also confirm our previous results that both populations should have very similar radial distribution and, furthermore, very similar structure. The similarity in the SBP for both populations also suggests that they are already in a well-mixed state.

4.2.10. Spatial distributions

In our previous study of M22 (Lee 2015), we showed that the spatial distributions can provide a very powerful diagnostics to compare the structural properties between MSPs, which are closely related to and affected by their internal kinematics. Here, we explore the spatial distributions of RGB stars in M5.

In the top panels of Figure 17, we show the projected spatial distributions of the CN-w and the CN-s populations in M5. In the figure, the offset values of the projected right ascension and the declination in the units of arcsec were calculated using the transformation relations given by van de Ven et al. (2006),

$$\begin{aligned} \Delta\text{R.A.} &= \frac{648000}{\pi} \cos \delta \sin \Delta\alpha, \\ \Delta\text{decl.} &= \frac{648000}{\pi} (\cos \delta \cos \delta_0 - \cos \delta \sin \delta_0 \cos \Delta\alpha), \end{aligned} \quad (5)$$

where $\Delta\alpha = \alpha - \alpha_0$ and $\Delta\delta = \delta - \delta_0$, and α_0 and δ_0 are the coordinate of the center. For our calculations, we adopted the coordinate for the cluster center measured by Goldsbury et al. (2010).

In the lower panels of the figure, we show smoothed density distributions of RGB stars along with iso-density contours for each population. For the smoothed density distribution of each population, we applied a fixed Gaussian kernel estimator algorithm with a full-width at the half-maximum (FWHM) of $52''$ (Silverman 1986). We show the FWHM of our Gaussian kernel in the lower left panel of the figure. To derive the iso-density contour for each population, we applied the second moment analysis (Dodd & MacGillivray 1986; Stone 1989) and we show the iso-density contour lines for 90, 70, 50, and 30% of the peak values for both populations.

The projected distribution of the CN-s population is more spatially elongated than that of the CN-w population. The major axis of the projected density profile of the CN-s population is placed along the NW-SE direction. In Table 8, we show the axial ratio, b/a , and the ellipticity, $e (= 1 - b/a)$. The radial distributions of the axial ratio and the ellipticity can be found in Figure 18. As shown, the ellipticity of the CN-s population is much larger than that of the CN-w population up to $\approx 2r_h$ of the cluster. This is not expected or difficult to anticipate from the cumulative radial distributions or the SBPs of each population as shown in Figures 14 and 16. Our results vividly demonstrate the importance of using the spatial distribution at rather large radial distance to examine the structural differences between the MSPs in GCs. As will be shown below, it is believed that the elongated projected spatial distribution of the CN-s RGB population is inextricably linked with its fast projected rotation.

4.2.11. Projected Rotations

In our previous work (Lee 2015), we showed that the peculiar GC M22 have different projected rotations between the two populations, providing a strong constraint to the formation scenario of M22. The rotation of M5 has not been reported yet, especially for the individual stellar populations in M5. Using the radial velocity measurements by Carretta et al. (2009), we explore the projected rotation of RGB stars in each population.

We estimated the amplitude of the mean rotation of the cluster using the method described by Lane et al. (2009). Assuming an isothermal rotation, the mean rotation can be measured by dividing the cluster in half at a given position angle and calculating differences between the average velocities in the two halves. During our calculation, we used the RGB stars within $3'$ from the cluster's center, which is about the largest radius of the ellipse that we showed in Figure 18. We repeated this calculation by increasing the position angle of the boundary of the two halves by 10° . Then the net rotation velocity is the half of the amplitude of the sinusoidal function in the differences between the average velocities in the two halves.

In Figure 19, we show the differences in the mean radial velocities as a function of the position angle (West = 0° and North = 90°) along with the best-fitting sine function. We obtained the mean rotation velocity of $1.7 \pm 0.7 \text{ km s}^{-1}$ for all RGB stars and the position angle of the equator of 128° (i.e., along the NE-SW direction). In the middle and the bottom panels, we show plots of differences in the mean radial velocities for the *Ca-w* and the *Ca-s* populations. We obtained the mean rotation of $1.0 \pm 1.7 \text{ km s}^{-1}$ with the position angle of 51° for the CN-w population and $2.2 \pm 0.9 \text{ km s}^{-1}$ with the position angle of 136° for the CN-s population. It is thought that the CN-w population does not appear to have a net projected rotation, while CN-s population shows a substantial net projected rotation. The position angle of the axis of the projected rotation for the CN-s population is 136° (i.e., along the NE-SW direction), which is in accord with the projected spatial distribution of the CN-s population if its elongated shape is mainly due to its fast rotation.

In the future, more systematic radial velocity measurements of M5 RGB stars will be very desirable and will shed more light on the kinematic property of each population.

4.3. Asymptotic giant stars

Until recently, the AGB populations in the GC systems were rather neglected, despite of their intrinsic brightness. However, in the context of the MSP, the importance of the AGB star became greater (e.g. see Pilachowski et al. 1996; Sneden, Ivans, & Kraft 2000). For example, the AGB stars can provide a wonderful opportunity to understand the stellar structure and evolution of the low mass stars (e.g., see Norris et al. 1981; Campbell et al. 2013). For decades, it has been known that some GCs have different CN contents in the AGB phase than in the RGB phase. In their pioneering study, Norris et al. (1981) found that NGC 6752 does not appear to have CN-s AGB stars, while the CN-s RGB stars are the major component, which led them to propose that the CN-s RGB stars failed to evolve into the AGB phase (the so-called AGB-manqué stars). Interestingly, M5 is in the opposite case. Smith & Norris (1993) found a deficiency of the CN-w AGB stars in M5.

The trouble with the AGB stars is that they are much rarer than their progenitors; the MS, RGB and HB stars. For example, the typical number ratio of the AGB stars to the RGB stars in Galactic GCs is very small, $n(\text{AGB})/n(\text{RGB}) \approx 0.1 - 0.2$, depending on the definition of the AGB and the RGB phases (e.g.,

see Buzzoni et al. 1983; Gratton et al. 2010). As a consequence, statistical fluctuations introduced from the small number statistics can not be avoided. The situation in the spectroscopic study of AGB stars will be worse, because the AGB stars in the central part of GCs would be very difficult to observe, which is the case for M5 as we will show below. In this regard, our cn_{JWL} index can open a new era on the MSP study of the AGB stars, because our approach is applicable to the central part of the cluster, where the spectroscopic method has an ultimate limitation that can not be avoided due to crowdedness. If so, our results can provide the complete census on the true nature of the MSP of the AGB stars.

4.3.1. *The relative AGB frequency, $n(AGB)/n(RGB)$, as an indicator for the missing AGB population in GCs*

In Figure 20, we show plots of the relative AGB frequencies against the HB type (HBT), metallicity, absolute integrated magnitude and the minimum mass along the HB using the data by Harris (1996) and Gratton et al. (2010). In their recent study, Gratton et al. (2010) proposed that the relative AGB frequency is correlated with the minimum mass along the HB and metallicity. We calculated the linear correlations and show our results in Table 9, confirming what Gratton et al. (2010) proposed.

The relative AGB frequency as functions of the HBT or metallicity may depend on various factors; the metallicity dependency on the time spent on the RGB and the AGB evolutionary phases, the mass loss, and etc. If our linear correlations between the relative AGB frequency and other parameters are mainly related to the relative fraction of the AGB-manqué stars, our results can be used to estimate the missing AGB populations in a given GC. If so, Figure 20 can provide a strong line of evidence that the missing AGB population owing to the presence of the AGB-manqué, preferentially in the CN-s population with enhanced helium abundances, would be negligible in M5, since M5 is located near the upper limit of the relative AGB frequency. In other word, the AGB stars in both populations in our study should represent the complete sample in terms of the stellar evolution.

4.3.2. *Multiple AGB populations in M5*

It is fortunate that AGB stars in GCs are not hot enough to suppress the CN band formation in their atmospheres. Therefore, if there exists a spread or a variation in the CN abundance among AGB stars, we should be able to tell the abundance differences using our cn_{JWL} index. However, at a fixed visual magnitude, the AGB stars are slightly warmer than the RGB stars by 100 - 200 K and, therefore, the CN band absorption strengths in the AGB stars are expected to be weaker than those in the RGB stars due to the temperature effect.⁸ Therefore, it is expected that if there exist MSPs in the AGB phases, the separation in our cn_{JWL} index between CN-w and the CN-s AGB populations would become smaller than that in the RGB populations.

In Figure 21(a-b), we show the $(b - y)$ versus V and the cn_{JWL} versus V CMDs for AGB stars in M5, where the discrete double AGB sequences in the cn_{JWL} index can be clearly seen as in the RGB sequence. Note that we do not include the AGB stars near the RGB tip, where it becomes difficult to tell the AGB from

⁸The AGB stars have slightly larger surface gravities than the RGB stars do. However, the CN band is rather insensitive to the change in the surface gravity.

the RGB sequences. Also shown are the six AGB stars⁹ studied by Smith & Norris (1993), who performed a low resolution spectroscopic study to investigate the CN distributions of the RGB and the AGB stars in M5. Their $S(3839)$ measurements for the RGB and the AGB stars are in excellent agreement with our cn_{JWL} index, although the extent of the separation between the two populations is smaller in the AGB phase, which is thought to be the temperature effect as we mentioned before. This was also noted by Smith & Norris (1993), who found a smaller spread of CN band strengths in the AGB stars than in the RGB stars in M5. As shown in the figure, the cn_{JWL} values of the CN-w AGB and RGB stars are in accord with each other, while the mean cn_{JWL} value of the CN-s AGB stars are slightly smaller than that of the CN-s RGB stars.

The high resolution spectroscopic study of the AGB stars in M5 by Ivans et al. (2001) also confirms that our cn_{JWL} index works nicely for the MSPs of the AGB stars. In Figure 22, we show the cn_{JWL} versus V CMD and the Na-O anticorrelation of the AGB stars studied by Ivans et al. (2001). Similar to what showed for the RGB stars in Figure 9, the CN-s AGB stars based on our cn_{JWL} index have lower oxygen and higher sodium abundances than the CN-w AGB star do. Therefore, the CN-w AGB stars shown in Figures 21 and 22 are equivalent to the CN-w RGB stars.

4.3.3. Radial distributions of AGB stars

Smith & Norris (1993) first noted that the majority of the AGB stars in their sample (seven out of eight) belongs to the CN-s population in M5 (see also Smith, Modi, & Harmen 2013). As discussed before, the lack of the CN-s AGB population in NGC 6752 can be naturally explained by the presence of the AGB-manqué stars. However, the deficiency of the CN-w AGB population in M5 can not be easily explained by the theory of the stellar evolution of the low-mass stars. It is thought that the deficiency of the CN-w AGB stars is likely originated from the stochastic truncation of the CN-w AGB stars in the outer region, which ultimately lead the CN-w AGB population to be more centrally concentrated.

First, we calculate the number ratio between the two AGB populations. Assuming a bimodal distribution, we applied the EM algorithm for the two-component Gaussian mixture distribution model to calculate the contributions from two groups of stars. In an iterative manner, we derive the probability of individual AGB stars for being the CN-w and the CN-s AGB populations. We obtained the number ratio of $n(\text{CN-w}):n(\text{CN-s}) = 21:79 (\pm 7)$, which is marginally consistent with that from RGB stars, $n(\text{CN-w}):n(\text{CN-s}) = 29:71 (\pm 2)$. The relative fraction of the CN-w AGB stars by Smith & Norris (1993), $n(\text{CN-w}):n(\text{CN-s}) = 1:7$, is considered to be very small compared to ours.

In Figure 23(a), we show the spatial distributions of the CN-w and the CN-s AGB stars, along with the six AGB stars studied by Smith & Norris (1993). In the figure, it is evident that the CN-s AGB stars are preferentially located along the NW-SE direction, consistent with the spatial distribution of the CN-s RGB stars. This also indicates that both the AGB and the RGB stars may share the same structural and, furthermore, kinematical properties. We also note that the CN-w AGB stars are more centrally concentrated than the CN-s AGB stars are, which can be clearly seen in Figure 23(b). We performed a K-S test and we obtained the significance level of being drawn from the identical population is 0.054, with a K-S discrepancy of 0.390, suggesting that they are likely drawn from the different parent distributions.

In Figure 23(c-d), we show comparisons of the radial distributions of the AGB populations and those of

⁹Since Smith & Norris (1993) did not provide the positions of the two AGB stars (S344 and S445) in their Table 1, we were not able to match them in our results.

the RGB populations. For the CN-w population, the radial distribution of the AGB stars does not agree with that of the RGB stars. Our K-S test may suggest that the CN-w RGB and AGB stars are likely drawn from different parent distributions, with the significance level of being drawn from the identical population of 0.073. On the other hand, the radial distribution of the CN-s AGB stars is in excellent agreement with that of the CN-s RGB stars. Our K-S test strongly suggest that the two populations are most likely drawn from the identical parent distribution, with the significance level of 0.662. Again, our statistical tests indicate that the CN-s AGB and RGB stars share the same structural property, while the CN-w AGB and RGB stars do not. As shown in Figures 21 and 22, the number ratio of the CN-w AGB stars is small and the radial distribution of the CN-w AGB stars may suffer from the unavoidable effect from the small number statistics.

The cumulative distributions for the CN-w and CN-s AGB stars look different, as we already showed in Figure 23(b). The use of the cumulative distribution has some advantages in the statistical evaluations of the data, however, some subtle differences can be missed with it. In Table 10, we show the number ratios of the AGB to the RGB stars for each population at different radial zones. Note that these number ratios are not the same as those by Gratton et al. (2010), as already shown in Figure 20, who adopted different definitions of the AGB and the RGB phases in their calculations. In the table, the number ratios of the AGB stars to the RGB stars for both populations are in excellent agreement in the central part of the cluster ($r \leq r_h$), with the number ratios of 0.048 with slightly different estimated errors. The number ratio of the CN-s population in the outer part, $r_h < r \leq 5r_h$, is also in good agreement, with that of 0.056 ± 0.012 . However, that of the CN-w population in the outer part is significantly smaller, with the number ratio of 0.028 ± 0.014 , and does not agree with others. Therefore, what makes different cumulative distribution for the CN-w population is the outer part of the cluster, where the number of stars is very small.

In order to see if the radial distribution of the CN-w AGB stars is intrinsically different from those of others, we also undertook a randomization test. We calculated the empirical distributions of the mean value of relative fraction of the CN-w AGB and the CN-w RGB populations in two radial zones, the inner region ($r \leq r_h$) and the outer region ($r_h < r \leq 5r_h$), and we show our results in Table 11 and Figure 24. In the inner part of the cluster, there appears to be no difference between the AGB and RGB stars in the relative fraction of the CN-w population. The mean values of the relative fraction of the CN-w population in the empirical distributions for the AGB and the RGB stars are almost identical, 0.302 ± 0.036 and 0.301 ± 0.063 , respectively. In the outer part of the cluster, however, the empirical distributions for the AGB and the RGB stars are significantly different each other, with the mean values of 0.123 ± 0.017 for the AGB and 0.282 ± 0.061 for the RGB stars. It should be reminded that our CN-w AGB fraction for the outer part is exactly the same as what Smith & Norris (1993) found for the cluster, $n(\text{CN-w}):n(\text{CN-s}) = 1:7$. The total distributions ($r \leq 5r_h$) for both phases are marginally in agreement each other, with the mean values of 0.221 ± 0.057 for the AGB and 0.291 ± 0.064 for the RGB stars.

The astrophysical origin of the deficiency of the CN-w AGB stars in the outer part of the cluster is not clear. It is difficult to believe that the CN-w AGB stars in the outer region of the cluster had been preferentially removed from the cluster in the course of the relaxation process, for example. It is naturally expected that the AGB stars simply do not have enough time to be affected by the relaxation process due to their very short life times on the AGB phase. Also they used to be more massive in the past than the RGB stars at present time, which can lead the AGB stars to sink to the central part of the cluster if the two-body relaxation took place. The tidal effect from our Galaxy cannot explain the situation, since the tidal effect should have affected both the AGB and the RGB stars at the same time, but the CN-w or the CN-s RGB stars do not show any sign of the deficiency in the outer region of the cluster.

Instead, we suspect that the fundamental and unavoidable stochastic truncation due to the small number

of stars can explain the deficiency of the CN-w AGB stars in the outer region of M5. For example, adding three CN-w AGB stars in the outer region of the cluster ($r_h < r \leq 5r_h$) can result in the mean value of 0.252 ± 0.083 , dramatically mitigating the discrepancy.

Finally, our number statistics also indicates that the AGB-manqué population in M5 can be negligible, as already shown in Figure 20, seeing that the number ratios of the AGB to the RGB populations for the CN-s population is in excellent agreement with that of the CN-w population in the central part of the cluster. Therefore, our results may set an observational constraint on the emergence of the AGB-manqué stars.

5. SUMMARY AND DISCUSSIONS

The understanding of the formation of the GCs with MSPs is one of the outstanding problems in the near field cosmology, however, we are still in the period of the stamp collecting. In this work, we provided very important observational lines of evidence to shed more light on the true nature of the MSPs in GCs.

Throughout our decade long painstaking effort, we invented new filter systems, which allow us to measure the heavy and the CN abundances simultaneously. Our new cn_{JWL} index can provide a very powerful means to probe the MSPs in the RGB and the AGB stars in the Galactic GC systems. Apparently, among other photometric indices being used in the ground-based observations, our cn_{JWL} is the only reliable photometric index that can accurately distinguish MSPs in normal GCs. Furthermore, our approach can complement the intrinsic weaknesses of the powerful instruments that currently used in the field of the MSPs in GCs; for example, the photometric study using the *HST* (a small FOV) and the spectroscopic study using the *VLT* (an incomplete sampling in the central part of GCs). The FOV of our typical instrument setup is about 55 times larger than that from the WFC3/*HST* and our method can easily be used in the central part of GCs. The large FOV is critical in the statistical study of the MSPs in GCs and in understanding the formation of such GCs. For example, Vesperini et al. (2013) discussed that the local relative number ratio between the MSPs can be different from the global number ratio until the achievement of the complete mixing. Therefore the large area of the spatial coverage is essential to ensure the correct population number ratios, although M5 does not show any radial gradient in the population number ratio.

As a pilot work, we investigated the MSPs of the RGB and the AGB in M5, an archetype of GCs with a CN bimodality. Our multi-color CMDs showed for the first time that our cn_{JWL} index exhibits the discrete double RGB and AGB sequences, while other indices known to trace the variations in the lighter elemental abundances, such as $m1$ and cy , do only show some spreads and trends, but fail to trace the accurate light elemental abundances. Using the EM algorithm, we obtained the number ratios of $n(\text{CN-w}):n(\text{CN-s}) = 29:71 (\pm 2)$ and $21:79 (\pm 7)$ for the RGB and the AGB, respectively, placing the CN-s population the major component of the cluster.

By comparing with previous results from low resolution spectroscopy by others (Briley et al. 1992; Smith & Norris 1993; Smith, Modi, & Harmen 2013), we showed that our cn_{JWL} index accurately traces the CN at $\lambda 3883 \text{ \AA}$ band absorption strengths so that our cn_{JWL} index can be used to derive the photometric $S(3839)$ or $\delta S(3839)$ and, furthermore, the photometric nitrogen abundances of RGB stars in M5. Our statistical test showed that M5 most likely has a bimodal nitrogen distribution. Using the linear correlation between our cn_{JWL} index versus $[\text{N}/\text{Fe}]$ measurements by Briley et al. (1992), we derived the photometric nitrogen abundances for individual RGB stars. On the other hand, the photometric nitrogen abundances from other indices, $m1$ and cy , failed to reproduce the nitrogen abundance distribution by Briley et al. (1992).

Comparisons with the previous high resolution spectroscopic studies by Ivans et al. (2001) and Carretta et al. (2009) also confirmed that our cn_{JWL} index is a very powerful means to explore the MSPs in the RGB and in the AGB. The CN-w population from our photometry has higher oxygen and lower sodium abundances both in the RGB and the AGB, while the CN-s population has lower oxygen and higher sodium abundances. From the photometric point of view, there is no difference between the intermediate and the extreme populations defined by Carretta et al. (2009), which was also pointed out by Smith, Modi, & Harman (2013) in their study of M5 using the $\delta S(3839)$. Perhaps, this may be due to somewhat arbitrary definitions of the intermediate and the extreme populations.

One of the astounding results is the discontinuities in the cn_{JWL} versus [O/Fe] and the cn_{JWL} versus [Na/Fe] relations (i.e., the discontinuous [N/Fe] versus [O/Fe] and the [N/Fe] versus [Na/Fe] relations) between the CN-w and the CN-s populations, while no such discontinuity exists in the Na-O anticorrelations in GCs (e.g., see Carretta et al. 2009). The large sample size in our study allows us to detect these discontinuities more clearly than what Smith, Modi, & Harman (2013) first suspected in their limited number of sample. Our careful re-examination of the results by Yong et al. (2008) showed that NGC 6752 also exhibits such discontinuities in the [N/Fe] versus [O/Fe] and the [N/Fe] versus [Na/Fe] relations, which will be presented in our forthcoming paper (Lee 2017a, in preparation). The discontinuous chemical evolution in terms of the nitrogen abundances (while apparently continuous chemical evolution in terms of the oxygen and sodium abundances) in normal GCs may pose a difficult but crucial constraint on the GC formation scenario.

In order to probe the helium abundance, which is less well-known in GC stars, we investigated the visual magnitude of the RGB bump, finding that the V_{bump} magnitude of the CN-s population is slightly brighter than that of the CN-w population, $\Delta V_{\text{bump}} = 0.07 \pm 0.04$ mag. If real, the difference in the helium abundance between the two populations could be $\Delta Y = 0.028 \pm 0.016$, in the sense that the CN-s population is more helium enhanced. Then, the CN-s RGB stars are likely the progenitor of the blue HB populations in M5.

From the hiatus in our cn_{JWL} -[O/Fe] or the cn_{JWL} -[Na/Fe] relations, it is thought that the CN-s stars formed out of gas that already significantly experienced the proton capture processes at high temperature. Regardless of the candidates, helium also should be supplied to the proto-stellar medium for the CN-s population through such processes. Up to date, no age differences between the two populations in M5 has been reported yet. However, judging from the currently available HST photometry by Anderson et al. (2008), the age difference between the two populations should be very small, if any.

Our measurements of the centers of each population from the bright RGB stars using various methods suggest that both populations appear to have nearly the same position of the center. We examined the radial distributions of the two RGB populations, finding that both populations are likely drawn from the same parent population, which is also supported by the consistent SBPs of both populations. However, the spatial distributions tell a different story. The projected spatial distribution of the CN-s RGB population is more elongated along the NW-SE direction and, subsequently, has a significantly larger ellipticity than the CN-w RGB population. The spatial distribution of the CN-s RGB stars is apparently consistent with that of the CN-s AGB stars, suggesting they share the same structural and, furthermore, kinematical characteristics.

The more elongated spatial distribution of the CN-s population is in accord with the internal kinematics of the population. We measured the projected rotations of each population and we obtained that the CN-s population has a substantial net projected rotation while the CN-w population does not appear to show any net projected rotation. The equator of the projected rotation (i.e., the axis perpendicular to the rotation axis) and the major axis of the projected iso-density profile of the CN-s population are aligned well each

other along the NW-SE direction, suggesting that the rotation of the system is inextricably linked to the ellipticity profile of the population (see also Lee 2015).

For the first time, we presented the complete view of the MSPs of the AGB stars in M5. Thanks to the capability of distinguishing MSPs in the dense stellar environment, our approach is easily applicable to the central part of the cluster, where the spectroscopic method has an ultimate limitation due to crowdedness. Furthermore, our method can open a new era for the MSPs of AGB populations in GCs.

Using the number ratios of the AGB to the RGB stars by Gratton et al. (2010), we showed that the probability of the emergence of the AGB-manqué stars in M5 is negligibly small and, therefore, our measurements for the relative AGB fraction will be a complete set of data. We confirmed the earlier notion made by Smith & Norris (1993), who found a deficiency of the CN-w AGB stars. Our statistical tests indicated that the radial distribution of the CN-w AGB stars are very different from other groups of stars in the cluster. We proposed that the stochastic truncation due to the small number of the CN-w AGB stars in the outer part of the cluster is responsible for the deficiency of the CN-w AGB stars in M5.

Unlike other peculiar GCs, like ω Cen and M22 (Marino et al. 2011a,b; Lee 2015), each stellar population in M5 based on our cn_{JWL} index does not exhibit its own Na-O anticorrelation. Therefore, our results for the different spatial distributions and the projected rotations for the two populations in M5 may not support the merger scenario of the two normal GCs, each of which has its own Na-O anticorrelation. On the contrary, our results of the different physical properties for each population can be understood from the view presented by Bekki (2010), who proposed that the SG of stars (i.e., the CN-s population in our work in the context of the self-enrichment scenario) formed from the gas expelled from the FG of stars (i.e., the CN-w population) in the central part of the cluster can have the flattened structure with a fast rotation.

The relaxation time scale at the half-light radius for M5 is less than 3 Gyr (Harris 1996) and it is significantly smaller than the age of the cluster, 11.50 ± 0.25 Gyr (VandenBerg et al. 2013). However, the recent N -body numerical simulations by Vesperini et al. (2013), for example, showed that the time required to achieve the complete mixing can be about at least 20 half-mass relaxation time. During the course of the long-term dynamical evolution of GCs with MSPs, any structural differences between the MSPs are expected to be gradually eliminated. From this view, the discrepancy between the radial and the spatial distributions of the MSPs in M5 may pose a somewhat contradictory problem. The similarity in the radial distributions of the both populations with the flat number ratios against the radial distance and with the same positions of the centers, can be a strong observational line of evidence of the complete mixing, while the very different spatial distributions with different internal kinematics may suggest that they are yet to be homogenized.

It is not clear if the homogenization in the radial distributions between the MSPs works in different time scale than that in the spatial distributions or the internal kinematics. The rotation of the GC system is the least well-known subject. Some numerical simulations suggest that the rotation of the GC system gradually decreases with time due to the combined effect of two-body relaxation and mass-loss (e.g., see Wang et al. 2016). The substantial net rotation of the CN-s RGB population, while no net rotation of the CN-w RGB population, could be a strong observational line of evidence of incomplete mixing.

Perhaps, may the similarity in the radial distributions in both populations tell that they were governed by the tidal effect induced mass-loss? Our preliminary results for more than two dozen of normal GCs using our own ground-based photometry are against this hypothesis. As will be presented in our forthcoming paper (Lee 2017b, in preparation), we obtained the relative RGB number ratio between the MSPs of GC and we found that there is no correlation between the relative number ratios against the Galactocentric distances and the spatial locations or the kinematic properties of individual GCs in our Galaxy.

In the future, high precision photometry to examine the potential age differences between the two populations would be very desirable. At the same time, more systematic and extensive radial velocity measurements would undoubtedly help to shed more light on understanding the formation of M5.

J.-W. Lee acknowledges financial support from the Basic Science Research Program (grant no. 2016-R1A2B4014741) through the National Research Foundation of Korea (NRF) funded by the Korea government (MSIP) and from the Center for Galaxy Evolution Research (grant No. 2010-0027910). J.-W. Lee thanks Drs. Sbordone, Piotto, Milone, Nardiello and Lardo for providing synthetic spectra, *HST UV* and *SDSS* photometry for M5 and the anonymous referee for constructive comments. Finally, special thanks must go to Bruce W. Carney, who inspired the author of the paper over the years.

A. COMPLETENESS TESTS

In our earlier study of the peculiar globular cluster M22, we showed that our ground-based photometry is complete down to $V - V_{\text{HB}} \approx 4.35$ mag. However, the apparent central crowdedness (see Lee et al. 2014, for the definition) of M5 is about 6 times larger than that of M22 (Lee 2015) and the crowdedness of the central part of M5 could be a potential problem for ground-based observations.

To examine the completeness of our photometry, we performed a series of artificial star experiments. We generated 100 artificial star images using a FORTRAN program to distribute 200 stars in the inner region ($r \leq r_h$), 1000 stars in the intermediate region ($r_h < r \leq 3r_h$) and 1500 stars in the outer field ($3r_h < r \leq 5r_h$), by adopting the observed radial stellar number density and the luminosity profile in our study. The number of artificial stars added to the observed images is carefully chosen so as not to dramatically change the crowdedness characteristics between our data reduction procedures and our artificial star experiments.

We used the same data reduction procedures that we described in §3 and we derived the completeness fractions as a function of V magnitude. Our results are shown in Figure 25. Our experiments suggest that our photometry is complete down to $V = 18.0$ and 19.0 mag for the intermediate and the outer regions of M5, respectively. On the other hand, owing to the rather large apparent central crowdedness of M5, our photometry for the inner part of the cluster becomes incomplete at as bright as $V \approx 16.0$ mag, which is equivalent to $V - V_{\text{HB}} \approx 1.0$ mag. The incomplete detection of stars in the very dense central part of GCs is the intrinsic weakness of any ground-based photometry. However, we emphasize that incomplete detection of stars in the central part of M5 does not affect our results presented in this work, since the radial distribution of the number ratio between the CN-w and the CN-s remains flat as we already showed in Figure 14.

B. NEW STRATEGY OF DATA REDUCTIONS OF THE GROUND-BASED PHOTOMETRY USING THE PRIOR POSITIONAL INFORMATION FROM HST ACS PHOTOMETRY

Anderson et al. (2008) presented homogeneous *HST ACS* photometry for 65 Galactic GCs. Assuming their photometry is more complete than any other ground-based photometry, their results may provide a very useful means to examine the validity of our completeness tests using artificial stars presented above.

In Figure 26, we show the CMDs and positions of stars in M5 from *HST ACS* photometry by Anderson et al.

(2008). In panels (a–b), we show stars matched with our ground-based observations, while panels (c–d) are for stars not detected in our measurements. We also derived the completeness fraction at each magnitude bins and we show our results in panel (e).

Note that the effective FOV of the *HST ACS* survey program is about $3 \times 3'$, equivalent to the area with $r \lesssim r_h$ for M5. If our artificial star experiments correctly reflect the completeness fraction in M5, the completeness fraction shown in Figure 26(e) should be the same as Figure 25(a). However, our results may indicate that this is not the case. We carefully re-examined every step in our data reductions and the artificial star experiments, and we confirmed that our procedures are correct. We suspect that the widely practiced artificial star experiments with the empirical point-spread functions may overestimate the completeness fractions.

In order to improve our photometry, we updated the input star list by merging the star list returned from our ALLFRAME run and the *HST ACS* star list not detected in our ground-based observations, i.e., stars in Figure 26(c). We re-run ALLFRAME with this updated input star list and we show our measurements in Figure 27. As shown, our approach can significantly improve the detection rate in the central part of M5. However, the detection rate is still not complete in the magnitude level of our interest, $-2 \leq V - V_{\text{HB}} \leq 2$ mag, equivalent to $13.07 \leq V \leq 17.07$ mag. It is thought that this incomplete detection of stars from the extensive input star list mainly due the treatment of blended stars in ALLFRAME. The critical separation parameter in ALLFRAME is set to be $0.375 \times \text{FWHM}$ and any stars within this distance are considered to be blended. Therefore, the many stars added in our updated list are treated to be blended with pre-detected stars from our previous ALLFRAME run.

We estimated the influence of the undetected stars on the ground-based photometry. We calculated the contribution in the surface flux from the individual undetected nearby stars. During our calculation we adopted a Moffat-type model point-spread function (Moffat 1969; Stetson et al. 2003),

$$I(r) = \frac{I_0}{[1 + (\frac{r}{\alpha})^2]^2}, \quad (\text{B1})$$

where $\alpha = 0.7769 \times \text{FWHM}$ and we adopted the FWHM of $1''.2$. As shown in Figure 28, our simulations suggest that the residual flux from the undetected nearby stars could cause a magnitude excess of $\Delta V_{\Sigma \text{nei}} \approx 0.01$ mag at $V - V_{\text{HB}} = -2$ mag, ≈ 0.08 mag at V_{HB} , and ≈ 0.35 at $V - V_{\text{HB}} = +2$ mag. However, some caution is advised when interpreting the results of our simulations. The magnitude excess due to the undetected nearby stars, $\Delta V_{\Sigma \text{nei}}$, shown in the figure is what one would get without a proper background brightness subtraction. This could cause a serious and mostly irreparable problem in spectroscopy. In photometry, however, the undetected nearby stars in a dense environment are treated as diffuse background sources and, as a consequence, they increase the background brightness. The sky subtraction algorithm implemented in ALLFRAME appears to work great, judging by the fact that our V_{bump} measurements do not show any significant radial fluctuations as shown in Table 6. It should be reminded that the V_{bump} magnitudes between in the central and in the outer part of M5 are in excellent agreement to within 0.01 mag.¹⁰

Finally, a more robust test for the influence of the undetected stars can be found in Figure 29, where we show comparisons of the input magnitudes to the output magnitudes from our artificial star experiments. Our experiments show that the differences between the input and output magnitudes are spatially independent

¹⁰Our previous study of the RR Lyrae variables in NGC 6723 also confirms our result presented here. See Figure 17 of Lee et al. (2014) for the constancy of the RR Lyrae magnitudes in NGC 6723 against the radial distance from the center.

at the magnitude of our interest, $-2 \leq V - V_{\text{HB}} \leq 2.0$ mag, although the standard deviations of the mean in the inner part of M5 ($r \leq 1'$) are larger than those in the outer part.

We conclude that the incomplete detection of stars in the central part of M5 does not affect the results presented here; The number ratios between the two populations remain the same thanks to the absence of any radial variations of the number ratios. At the same time, the residual flux from the undetected nearby stars is well taken care of by ALLFRAME and does not hardly affect our magnitude measurements, such as the V_{bump} magnitudes of the both populations.

REFERENCES

- Anderson, J., Sarajedini, A., Bedin, L. R. et al. 2008, *AJ*, 135, 2055
- Anthony-Twarog, B. J., Laird, J. N., Payne, D., & Twarog, B. A. 1991, *AJ*, 101, 1902
- Bastian, N., Larmers, H. J. G. L. M., de Mink S. E. et al. 2013, *MNRAS*, 436, 2398
- Bastian, N., & Lardo, C. 2015, *MNRAS*, 453, 357
- Bekki, K. 2010, *ApJ*, 723, L99
- Bjork, S. R., & Chaboyer, B. 2006, *ApJ*, 64, 1102
- Briley, M. M., Smith, G. H., Bell, R. A., Oke, J. B., & Hesser, J. E. 1992, *ApJ*, 387, 612
- Buton, C., Copin, Y., Aldering, G. et al. 2013, *A&A*, 549, A8
- Buzzoni, A., Fusi Pecci, F., Buonanno, R., & Corsi, C. E. 1983, *A&A*, 128, 94
- Campbell, S. W., D’Orazi, V., Yong, D. et al. 2013, *Nature*, 498, 198
- Carretta E., Bragaglia, A., Gratton, R.G., Lucatello S., Cantanzaro G. et al. 2009, *A&A*, 505, 117
- Cassisi, S., & Salaris, M. 2013, *Old Stellar Populations: how to study the fossil record of galaxy formation* (Berlin:Wiley-VCH)
- Chun, M. S., & Freeman, K. C. 1979, *ApJ*, 227, 93
- Cummings, J. D., Geisler, D., Villanova, S., & Carraro, G. 2014, *AJ*, 148, 27
- Decressin T., Charbonnel C., & Meynet G. 2007, *A&A*, 475, 859
- De Mink, S. E., Pols, O. R., Langer, N., & Izzard, R. G. *A&A*, 507, L1
- Denissenkov, P. A., & Hartwick, F. D. A. 2014, *MNRAS*, 437, L21
- D’Ercole, A., D’Antona, F., Ventura, P., Vesperini, E., & McMillan, S. L. W. 2010, *MNRAS*, 407, 845
- D’Ercole, A., Vesperini, E., D’Antona, F., McMillan, S. L. W., & Recchi, S. 2008, *MNRAS*, 391, 825
- Dodd, R. J., & MacGillivray, H. T. 1986, *AJ*, 92, 706
- Dotter A., Sarajedini A., Anderson J. et al. 2010, *ApJ*, 708, 698
- Goldsbury, R., Richer, H. B., Anderson, J., Dotter, A., Sarajedini, A., & Woodley, K. 2010, *AJ*, 140, 1830
- Gratton, R. .G., D’Orazi, V., Bragaglia, A., Carretta, E., & Lucatello, S. 2010, *A&A*, 522, A77
- Gray, R. O., & Corbally, C. J. 2009, *Stellar Spectral Classification* (1st ed.; Princeton: Princeton Univ. Press)
- Harris, W. E. 1996, *AJ*, 112, 1487
- Ivans, I. I., Kraft, R. P., Sneden, C. et al. 2001, *AJ*, 122, 1438
- Johnson, C. I., & Pilachowski, C. A. 2010, *ApJ*, 722, 1373

- Lane R. R., Kiss, L. L., Lewis, G. F., Ibata, R. A., Siebert, A., Bedding, T. R. & Székely, P. 2009, MNRAS, 400, 917
- Lardo, C., Bellazzini, M., Pancino, E., Carretta, E., Bragaglia, A., & Dalessandro, E. 2011, A&A, 525, A114
- Lee, J.-W. 2010, MNRAS, 405, L36
- Lee, J.-W. 2015, ApJS, 219, 7
- Lee, J.-W. 2016, ApJS, 226, 16
- Lee, J.-W., Kang, Y.-W., Lee, J., & Lee, Y.-W. 2009a, Nature, 462, 480
- Lee, J.-W., Lee, J., Kang, Y.-W., Lee, Y.-W., Han, S.-I., Joo, S.-J., Rey, S.-C., & Yong, D. 2009b, ApJ, 695, L78
- Lee, J.-W., López-Morales, M., Hong, K., Kang, Y.-W., Pohl, B. L., & Walker, A. 2014, ApJS, 210, 6
- Lee, J.-W., & Pogge, R. 2016, JKAS, 49, 289
- Lee, Y.-W., Joo, J.-M., Sohn, Y.-J., Rey, S.-C., Lee, H.-c., & Walker, A. R. 1999, Nature, 402, 55
- Marino, A. F., Milone, A. P., Piotto, G. et al. 2011a, ApJ, 731, 64
- Marino, A. F., Sneden, C., Kraft, R. P. et al. 2011b, A&A, 532, A8
- Mathis, J. S., 1990, ARA&A, 28, 37
- McClure, R. D., & van den Bergh, S. 1968, AJ, 73, 313
- Milone, A. P., Marino, A. F., Piotto, G. et al. 2013, ApJ, 767, 120
- Milone, A. P., Piotto, G., Renzini, A. et al. 2017, MNRAS, 464, 3636
- Moffat, A. F. J. 1969, A&A, 3, 455
- Norris, J., Cottrell, P. L., Freeman, K. C., & Da Costa, G. S. 1981, ApJ, 244, 205
- Osborn, W. 1971, Observatory, 91, 223
- Pilachowski, C. A., Sneden, C., Kraft, R. P., & Langer, G. E. 1996, AJ, 112, 545
- Piotto, G., Milone, A. P., Bedin, L. R. et al. 2015, AJ, 149, 91
- Renzini, A., D'Antona, F., Cassisi, S. et al. 2015, MNRAS, 454, 4197
- Sandquist, E. L., Bolte, M., Stetson, P. B., & Hesser, J., E. 1996, ApJ, 470, 910
- Sbordone, L., Salaris, M., Weiss, A., & Cassisi, S, 2011, A&A, 534, A9
- Silverman, B. W. 1986, Density Estimation for Statistics and Data Analysis (Chapman & Hall/CRC, New York)
- Smith, G. H. 1987, PASP, 99, 67
- Smith, G. H., Modi, P. N., & Harmen, K. 2013, PASP, 125, 1287

- Smith, G. H., & Norris, J. E. 1993, *AJ*, 105, 173
- Snedden, C., Ivans, I. I., & Kraft, R. P. 2000, *Mem. Soc. Astron. Italiana*, 71, 657
- Stetson P. B. 1987, *PASP*, 99, 191
- Stetson P. B. 1994, *PASP*, 106, 250
- Stetson P. B. 1995, *DAOPHOTII User's Manual* (Victoria : Dominion Astrophys. Obs.)
- Stetson P. B., Bruntt, H., & Grundahl, F. 2003, *PASP*, 115, 413
- Stone, R. C. 1989, *AJ*, 97, 1227
- Trager, S. C., King, I. R., & Djorgovski, S. 1995, *AJ*, 109, 218
- Valcarce, A. A. R., Catelan, M., & Sweigart, A. V. 2012, *A&A*, 547, A5
- VandenBerg, D. A., Brogaard, K., Leaman, R., Casagrande, L. 2013, *ApJ*, 775, 134
- van de Ven, G., van den Bosch, R. C. E., Verolme, E. K., & de Zeeuw, P. T. 2006, *A&A*, 445 513
- Vesperini, E., McMillan, S. L. W., D'Antona, F., & D'Ercole, A. 2013, *MNRAS*, 429, 1913
- Wang, L., Spurzem, R., Aarseth, S. et al. 2016, *MNRAS*, 458, 1450
- Yong, D., Grundahl, F., Johnson, J. A., & Asplund, M. 2008, *ApJ*, 684, 1159
- Zacharias, N., Monet, D. G., Levine, S. E., et al. 2004, *AAS*, 205, 4815

Table 1. Spectral resolving powers for selected UV filters.

		Johnson		<i>HST</i>			<i>SDSS</i>		Wash.	Extended Strömgen				
		<i>U</i>	<i>B</i>	F275W	F336W	F438W	<i>u</i>	<i>g</i>	<i>C</i>	<i>u</i>	<i>v</i>	<i>Ca_{new}</i>	<i>JWL39</i>	<i>cn_{JWL}</i> [†]
λ_c	(nm)	367	436	275	337	432	354	477	391	349	411	395	390	388
$\Delta\lambda$	(nm)	66	94	50	55	70	57	137	110	30	19	9	18	9
$\lambda_c/\Delta\lambda$		5.5	4.6	5.5	6.1	6.1	6.2	3.5	3.6	11.6	21.6	43.8	21.7	43.1

$${}^\dagger cn_{JWL} = JWL39 - Ca_{new}$$

Table 2. Integration times (s).

CTIO*					New Filters			
<i>y</i>	<i>b</i>	<i>v</i>	<i>u</i>	<i>Ca</i>	<i>y</i> [†]	<i>b</i> [†]	<i>Ca</i> _{new} [†]	<i>JWL39</i> [‡]
2630	4010	2100	3900	9660	3785	8900	37400	13000

*4 × 4 inches filters provided by the CTIO, which have been used from 2007 to 2010 seasons.

[†]4 × 4 inches filters designed and owned by J.-W. Lee, which have been used from 2011 to 2014 seasons.

[‡]A 4 × 4 inches filter designed and owned by J.-W. Lee, which has been used from 2013 to 2014 seasons.

Table 3. Coefficients and the goodness of the fit between $S(3839)$ [and $\delta S(3839)$] by Briley et al. (1992) and cn_{JWL} , cy and $m1$.

Index		Slope [†]	Intercept [†]	p -value	ρ^{\ddagger}
cn_{JWL}	$S(3839)$	4.201 ± 0.907	0.512 ± 0.063	0.000	0.757
	$\delta S(3839)$	4.112 ± 0.369	0.463 ± 0.025	0.000	0.941
cy	$S(3839)$	0.051 ± 1.129	0.262 ± 0.242	0.965	0.011
	$\delta S(3839)$	1.063 ± 0.848	0.432 ± 0.182	0.228	0.299
δcy^1	$S(3839)$	2.596 ± 0.766	0.572 ± 0.086	0.003	0.647
	$\delta S(3839)$	1.471 ± 0.699	0.361 ± 0.079	0.052	0.466
$m1$	$S(3839)$	2.428 ± 0.613	-0.222 ± 0.006	0.001	0.704
	$\delta S(3839)$	0.924 ± 0.639	0.030 ± 0.129	0.172	0.337
$\delta m1^2$	$S(3839)$	-0.491 ± 1.724	0.276 ± 0.096	0.780	-0.071
	$\delta S(3839)$	1.173 ± 1.328	0.150 ± 0.074	0.390	0.216

[†] $S(3839)$ or $\delta S(3839) = \text{Intercept} + \text{Slope} \times \text{Index}$.

[‡]Pearson's correlation coefficient.

$$^1\delta cy = cy - (-4.030 - 0.480V - 0.015V^2)$$

$$^2\delta m1 = m1 - (3.050 - 0.329V + 0.009V^2)$$

Table 4. Coefficients and the goodness of the fit between selected color indices and the nitrogen abundance.

Index	V level	[N/Fe]			
		Slope [†]	Intercept [†]	<i>p</i> -value	ρ^{\ddagger}
<i>cn_{JWL}</i>	bright	11.887 ± 2.543	1.628 ± 0.183	0.009	0.919
	faint	14.544 ± 1.757	1.626 ± 0.124	0.000	0.940
	all	12.925 ± 1.576	1.562 ± 0.110	0.000	0.899
<i>cy</i>	bright	28.569 ± 9.798	7.607 ± 2.312	0.043	0.825
	faint	4.406 ± 3.308	1.569 ± 0.670	0.217	0.406
	all	3.433 ± 2.795	1.483 ± 0.599	0.237	0.294
<i>m1</i>	bright	13.134 ± 5.743	-2.520 ± 1.489	0.084	0.753
	faint	6.860 ± 6.599	-0.407 ± 1.072	0.326	0.327
	all	3.316 ± 2.075	0.113 ± 0.418	0.130	0.371

[†][N/A] = Intercept + Slope × color index.

[‡]Pearson's correlation coefficient.

Table 5. Coefficients and the goodness of the fit between $S(3839)$ [and $\delta S(3839)$] by Smith, Modi, & Harmen (2013) and cn_{JWL} .

	Slope [†]	Intercept [†]	p -value	ρ^{\ddagger}
$S(3839)$	5.196 ± 0.417	0.738 ± 0.029	0.000	0.892
$\delta S(3839)$	5.609 ± 0.435	0.641 ± 0.030	0.000	0.898

[†] $S(3839)$ or $\delta S(3839) = \text{Intercept} + \text{Slope} \times cn_{\text{JWL}}$.

[‡]Pearson's correlation coefficient.

Table 6. RGB bump V magnitudes

	CN-w	CN-s
$r \leq 1'$	15.032 ± 0.030	14.963 ± 0.030
$r > 1'$	15.043 ± 0.030	14.973 ± 0.030
all	15.038 ± 0.030	14.970 ± 0.030

Table 7. Centers of M5 measured from stars within $r \leq 3r_h$.

	Simple mean		Half-sphere		Pie-slice	
	$\Delta\alpha''$	$\Delta\delta''$	$\Delta\alpha''$	$\Delta\delta''$	$\Delta\alpha''$	$\Delta\delta''$
All	0.6	2.7	2.6	3.1	0.6	2.5
CN-w	8.2	5.1	9.5	0.6	6.5	0.5
CN-s	-2.5	3.2	0.6	1.5	-4.2	1.3

Table 8. Ellipse fitting parameters for M5 RGB stars.

	grid	θ	b/a	e
CN-w	0.9	91.8 ± 4.1	0.970 ± 0.049	0.030
	0.7	96.7 ± 3.5	0.979 ± 0.042	0.021
	0.5	18.2 ± 2.8	0.969 ± 0.034	0.031
	0.3	28.2 ± 2.1	0.962 ± 0.025	0.038
CN-s	0.9	22.2 ± 4.0	0.926 ± 0.046	0.074
	0.7	23.2 ± 3.4	0.915 ± 0.039	0.085
	0.5	25.0 ± 2.7	0.899 ± 0.030	0.101
	0.3	28.7 ± 1.9	0.879 ± 0.021	0.121

Table 9. Goodness of the fits between the relative AGB frequencies and other parameters.

	$\langle \frac{n(\text{AGB})}{n(\text{RGB})} \rangle$	HB Type		[Fe/H]		M_V		M_{min}	
		p -value	r^\dagger	p -value	r^\dagger	p -value	r^\dagger	p -value	r^\dagger
21 GCs ¹	0.084 ± 0.017	0.005	-0.589	0.015	0.522	0.213	0.284	0.000	0.750
20 GCs ²	0.086 ± 0.017	0.000	-0.731	0.003	0.635	0.421	0.191	0.000	0.714

[†]Pearson's correlation coefficient.

¹21 GCs studied using the HST by Gratton et al. (2010)

²Without NGC 2808

Table 10. Number ratios of the AGB to the RGB populations.

	$\frac{n[\text{AGB}(\text{CN-w})]}{n[\text{RGB}(\text{CN-w})]}$	$\frac{n[\text{AGB}(\text{CN-s})]}{n[\text{RGB}(\text{CN-s})]}$
$r \leq r_h$	0.048 ± 0.015	0.048 ± 0.010
$r_h < r \leq 5r_h$	0.028 ± 0.014	0.056 ± 0.012
$r \leq 5r_h$	0.035 ± 0.009	0.053 ± 0.007

Table 11. Relative fraction of the CN-w population from the bootstrap realization.

	$\langle \frac{n[\text{AGB}(\text{CN-w})]}{n(\text{AGB})} \rangle_{\text{BS}}$	$\langle \frac{n[\text{RGB}(\text{CN-w})]}{n(\text{RGB})} \rangle_{\text{BS}}$
$r \leq r_h$	0.302 ± 0.036	0.307 ± 0.064
$r_h < r \leq 5r_h$	0.123 ± 0.017	0.273 ± 0.060
$r \leq 5r_h$	0.221 ± 0.057	0.291 ± 0.064

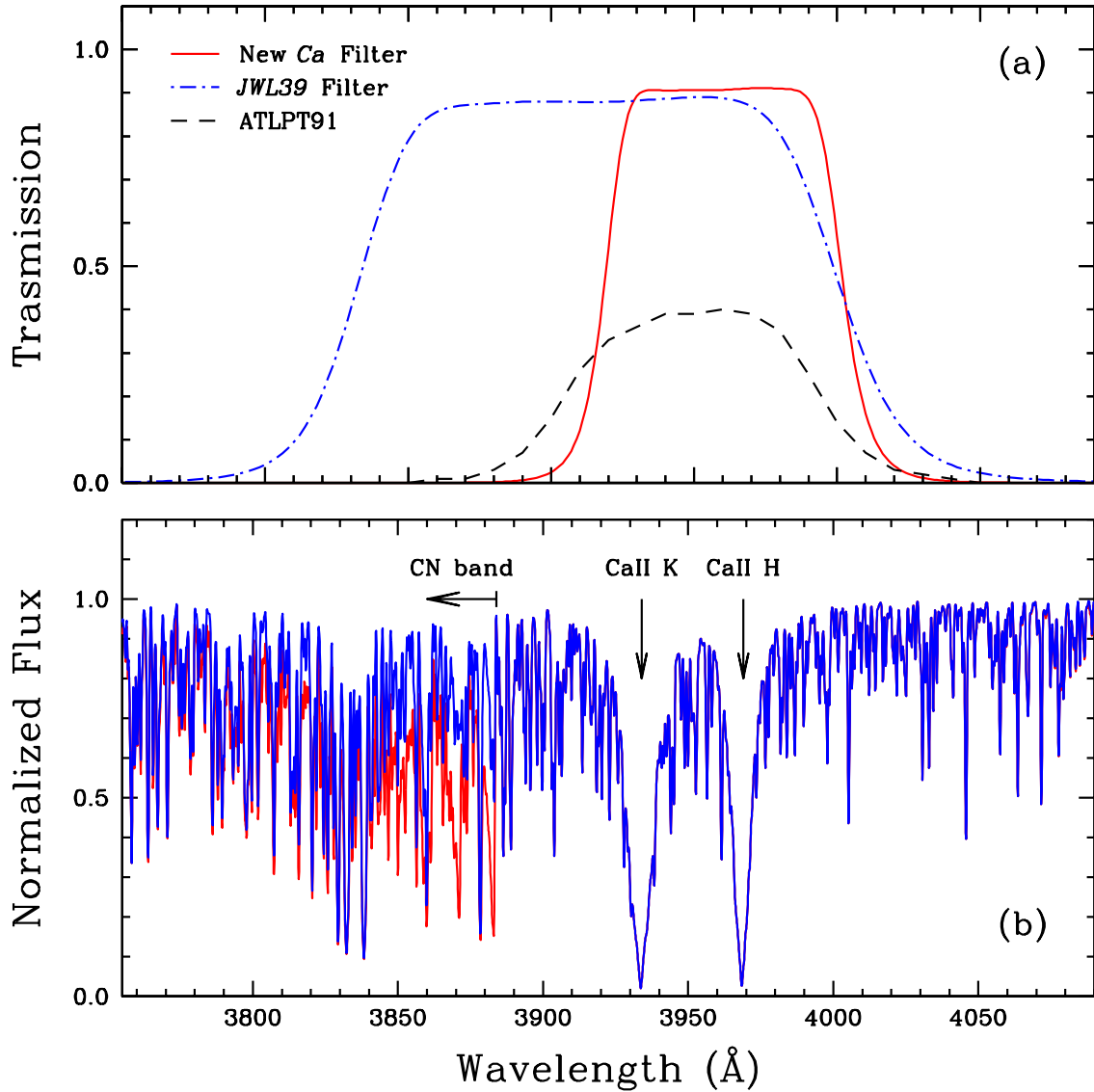


Fig. 1.— (a) Filter transmission functions for our new *Ca* and *JWL39* filters, measured with collimated beam. The CN absorption band at λ 3883 Å lies outside of the lower boundary of our new *Ca* filter. Note that our new *Ca* filter and that by Anthony-Twarog et al. (1991) have similar FWHMs, approximately 90 Å but our new *Ca* filter has a more uniform and high transmission across the passband, dropping more rapidly at both edges. Our new filter system, *JWL39*, is intended to measure CN band strength at λ 3883 Å, in conjunction with our new *Ca* filter. (b) Normalized synthetic spectra for the CN-w (the blue line) and the CN-s (the red line) RGB stars.

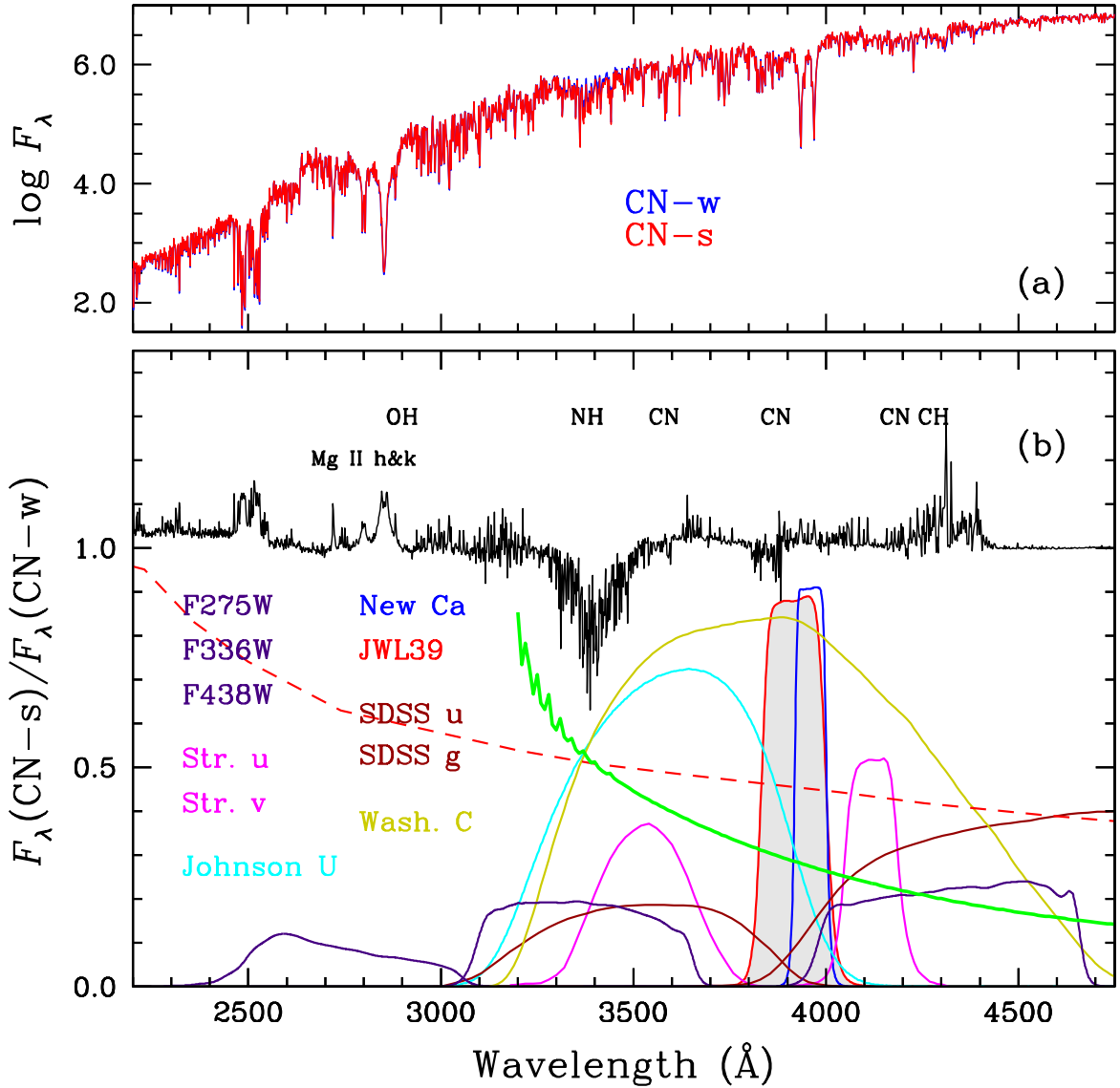


Fig. 2.— (a) A comparison of synthetic spectra for typical CN-w and CN-s RGB stars in GCs (Sbordone et al. 2011). (b) The flux ratio between the two spectra along with the transmission functions for various filter systems used in the UV and in the blue part of the visible light. The red dashed line denotes the interstellar extinction curve for $E(B - V) = 0.1$ mag (Mathis 1990) and the green solid line represents the atmospheric extinction curve for Mauna Kea, given in units of mag/airmass (Buton et al. 2013).

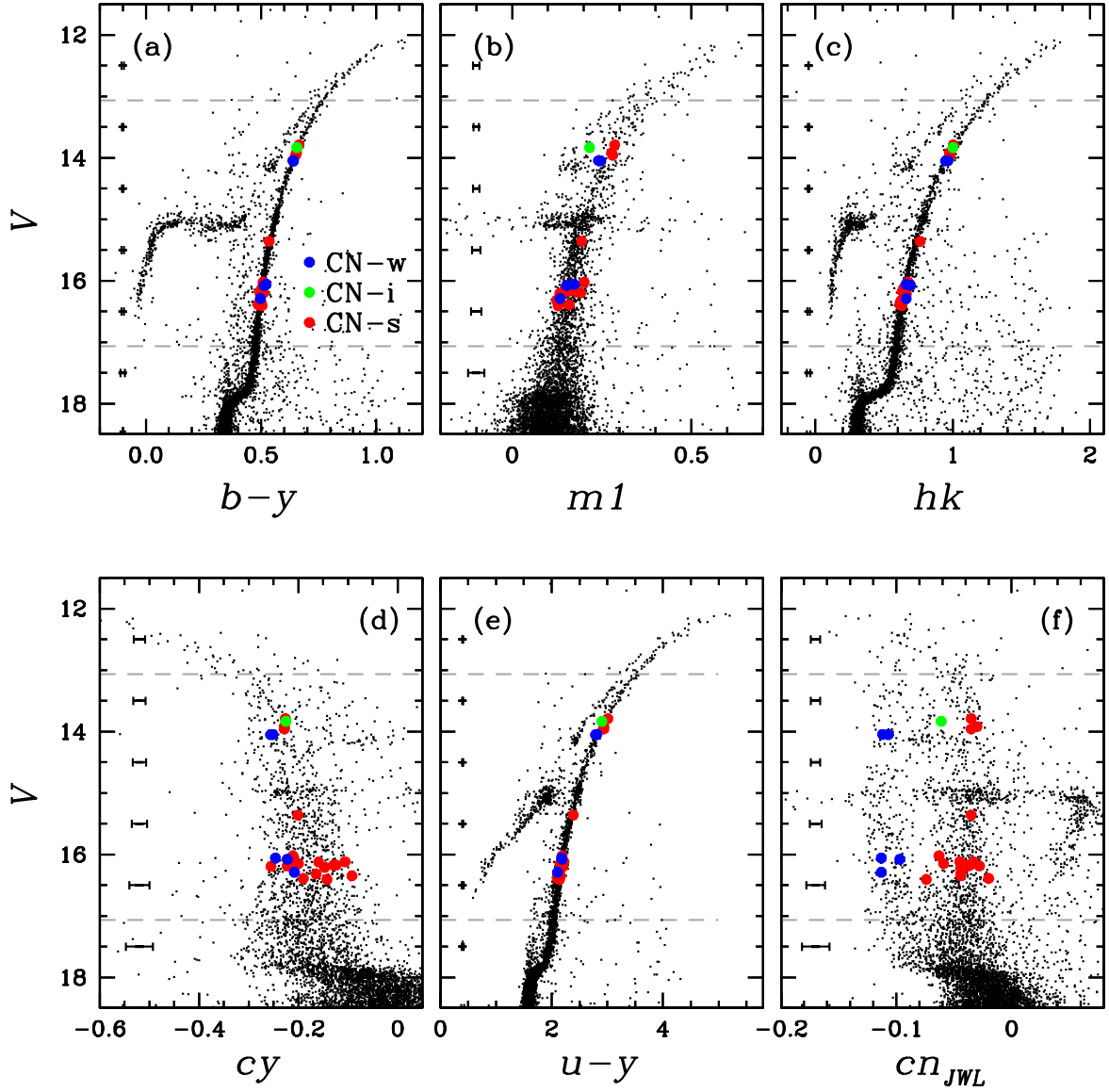


Fig. 3.— CMDs for good quality stars in M5 based on the separation index (Stetson et al. 2003). RGB stars studied by Briley et al. (1992) are also shown with filled circles. Blue filled circles denote the CN-w (the CN normal by Briley et al. 1992), a green one the intermediate CN absorption, red ones the CN-s RGB stars in M5. We show the measurement error of individual stars at given magnitude bins. The dashed horizontal lines are for $V - V_{\text{HB}} = \pm 2.0$ mag, with $V_{\text{HB}}(\text{M5}) = 15.07$ mag (Harris 1996). Note that the narrow single RGB sequence in $b-y$, $u-y$ and hk CMDs, while the very broad RGB sequence in $m1$ and cy CMDs, where the separation between different populations is ambiguous. On the other hand, the RGB stars in our cn_{JWL} index show distinct double sequences, consistent with the bimodal nitrogen distribution in M5.

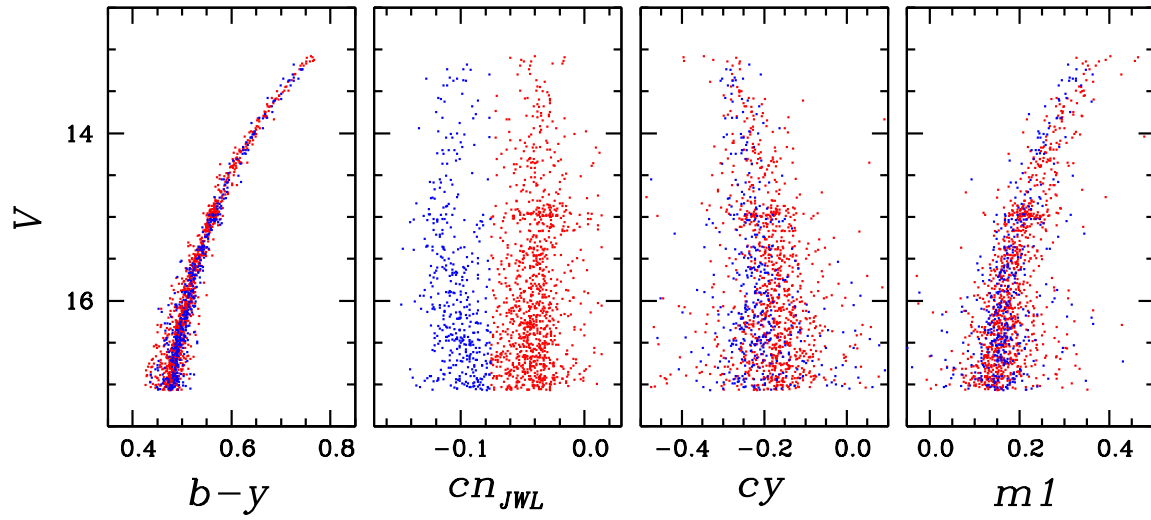


Fig. 4.— CMDs for all RGB stars with $V - V_{\text{HB}} = \pm 2.0$ mag. The blue dots denote the CN-w and the red dots the CN-s RGB stars in M5, based on the EM estimator for the two-component Gaussian mixture model for the cn_{JWL} distribution of the RGB stars.

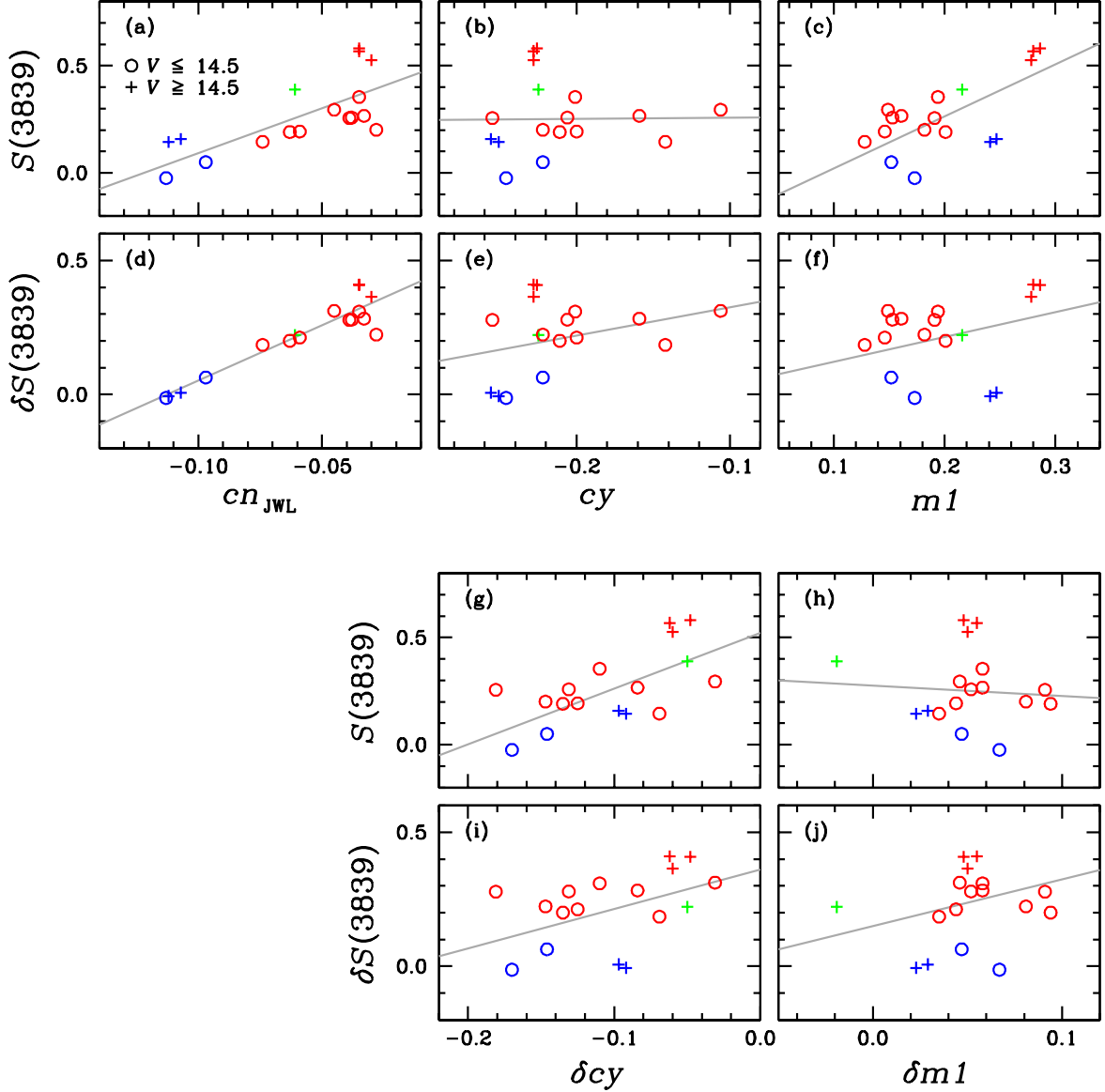


Fig. 5.— (a) – (c) Correlations between selected color indices and CN λ 3883 Å strength, $S(3839)$. The blue color denotes the CN-w, the green color the intermediate CN and the red color the CN-s (Briley et al. 1992). The grey solid lines are linear fits to the data. It can be clearly seen that our cn_{JWL} index is well correlated with $S(3839)$ in the whole magnitude level, while $m1$ and cy indices provide poor fit to the data (see Table 3). Also note that the scatters of the $S(3839)$ distribution around the fitted line in the $S(3839)$ versus cn_{JWL} relation are larger than those in the $\delta S(3839)$ versus cn_{JWL} relation, indicating that the gravity and temperature effects should be removed. (d) – (f) Correlations between selected color indices and the CN excess, $\delta S(3839)$. The linear fit between the cn_{JWL} and $\delta S(3839)$ is greatly improved. (g) – (j) Correlations between excesses in the color indices and $S(3839)$ and $\delta S(3839)$. Using color excesses δcy and $\delta m1$ does not have a net gain.

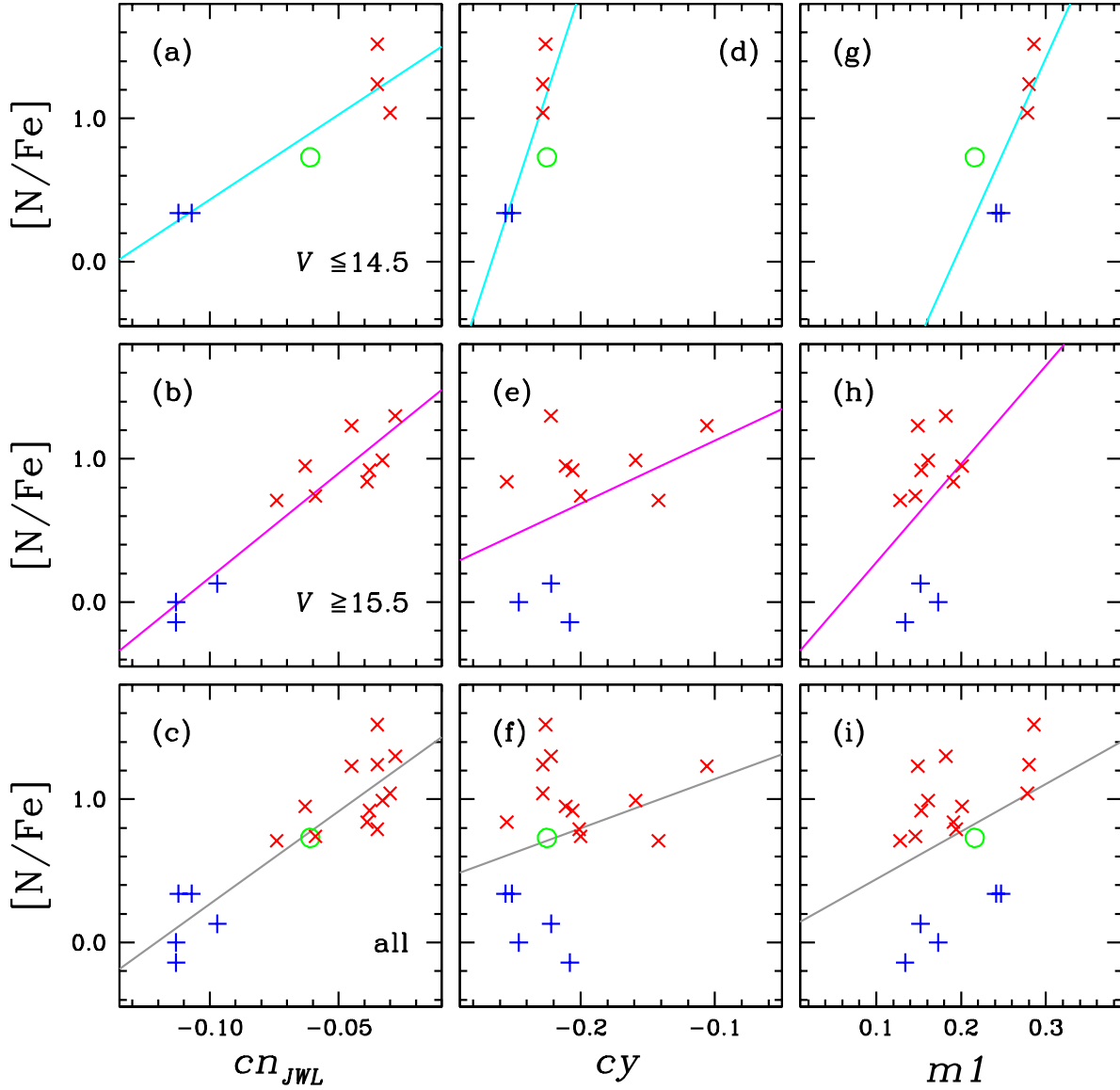


Fig. 6.— Correlations between selected color indices and nitrogen abundances of M5 RGB stars studied by Briley et al. (1992). We derive the linear fits for bright ($V \leq 14.5$ mag), faint ($V \geq 15.5$ mag) and all stars, and we show the fitted lines in each panel (see also Table 4). Note that our cn_{JWL} index is well correlated with nitrogen abundances in the whole magnitude level, while the cy and the $m1$ provide poor fit to the data in the faint magnitude regime.

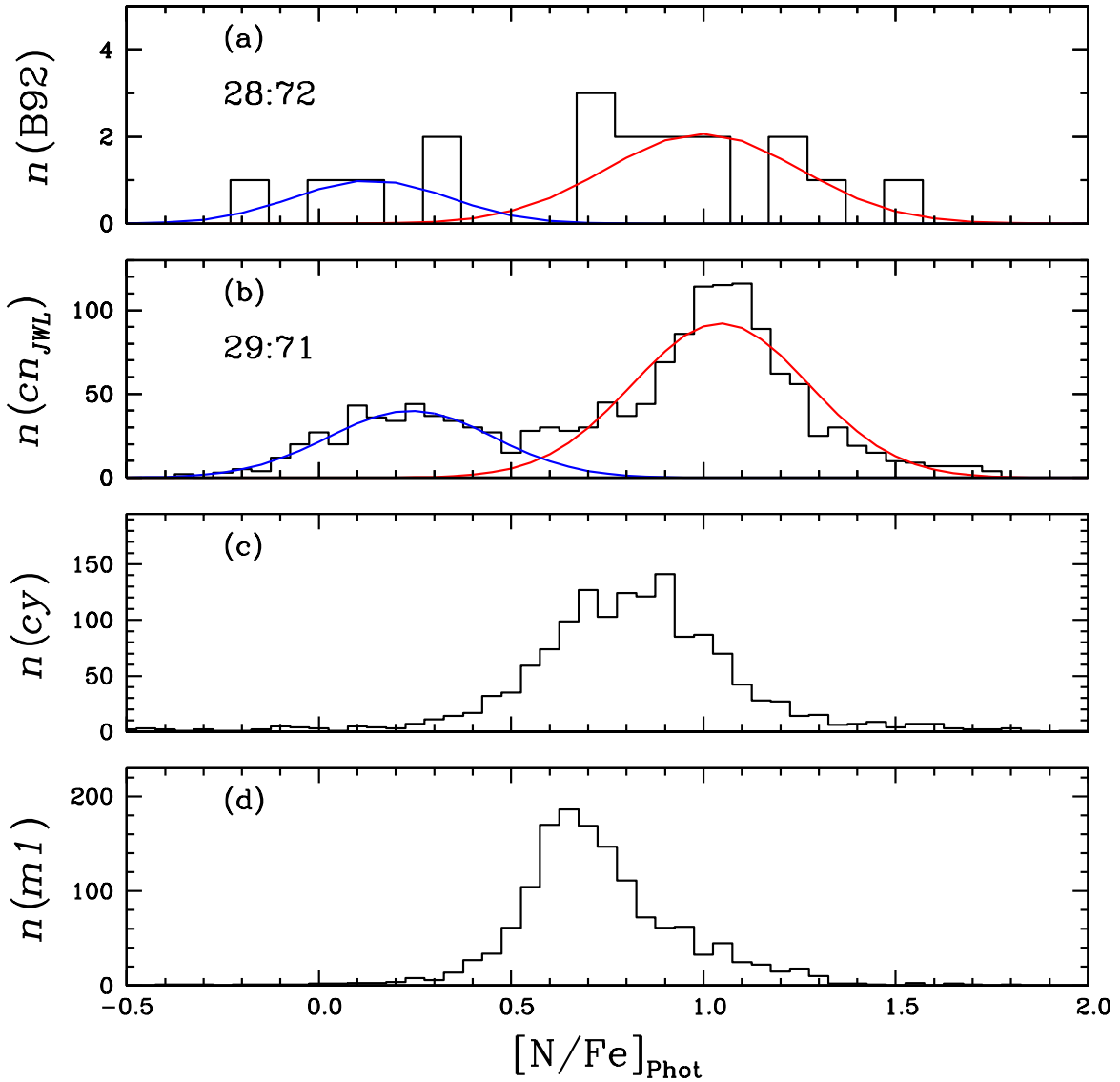


Fig. 7.— (a) The histogram of the nitrogen abundance by Briley et al. (1992). Our Hartigan’s dip test using the nitrogen abundance measurements by Briley et al. (1992) shows that the $[\text{N}/\text{Fe}]$ distribution of the M5 RGB stars is non-unimodal. The blue and red lines are for the N-normal and N-enhanced populations from the EM algorithm for the two-component Gaussian mixture distribution model. (b) The photometric nitrogen abundance distribution from our cn_{JWL} index using the relation given in Table 4, which is in excellent agreement with that of Briley et al. (1992). (c)–(d) The photometric nitrogen abundance distributions from cy and $m1$ indices, which fail to reproduce that of Briley et al. (1992).

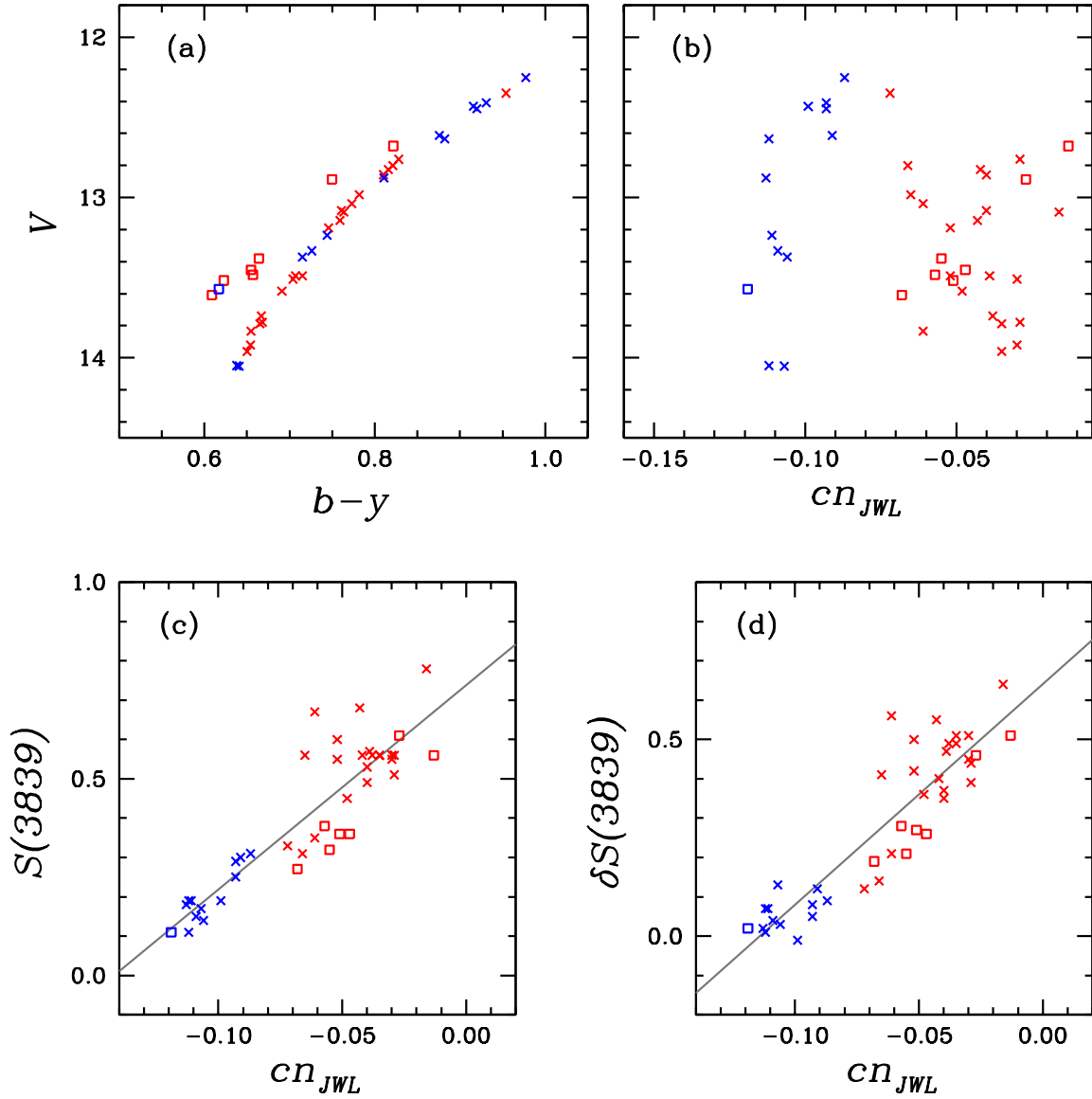


Fig. 8.— (a) The $(b-y)$ versus V CMD for the stars studied by Smith, Modi, & Harmen (2013). The crosses are for the RGB stars and the open squares for the AGB stars. The blue color denotes the CN-w population, while the red color the CN-s population. (b) The cn_{JWL} versus V CMD, where the distinct double AGB sequences are evident. (c) A plot of $S(3839)$ versus cn_{JWL} . (d) A plot of $\delta S(3839)$ versus cn_{JWL} . Note that our cn_{JWL} index correlates nicely with both $S(3839)$ and $\delta S(3839)$.

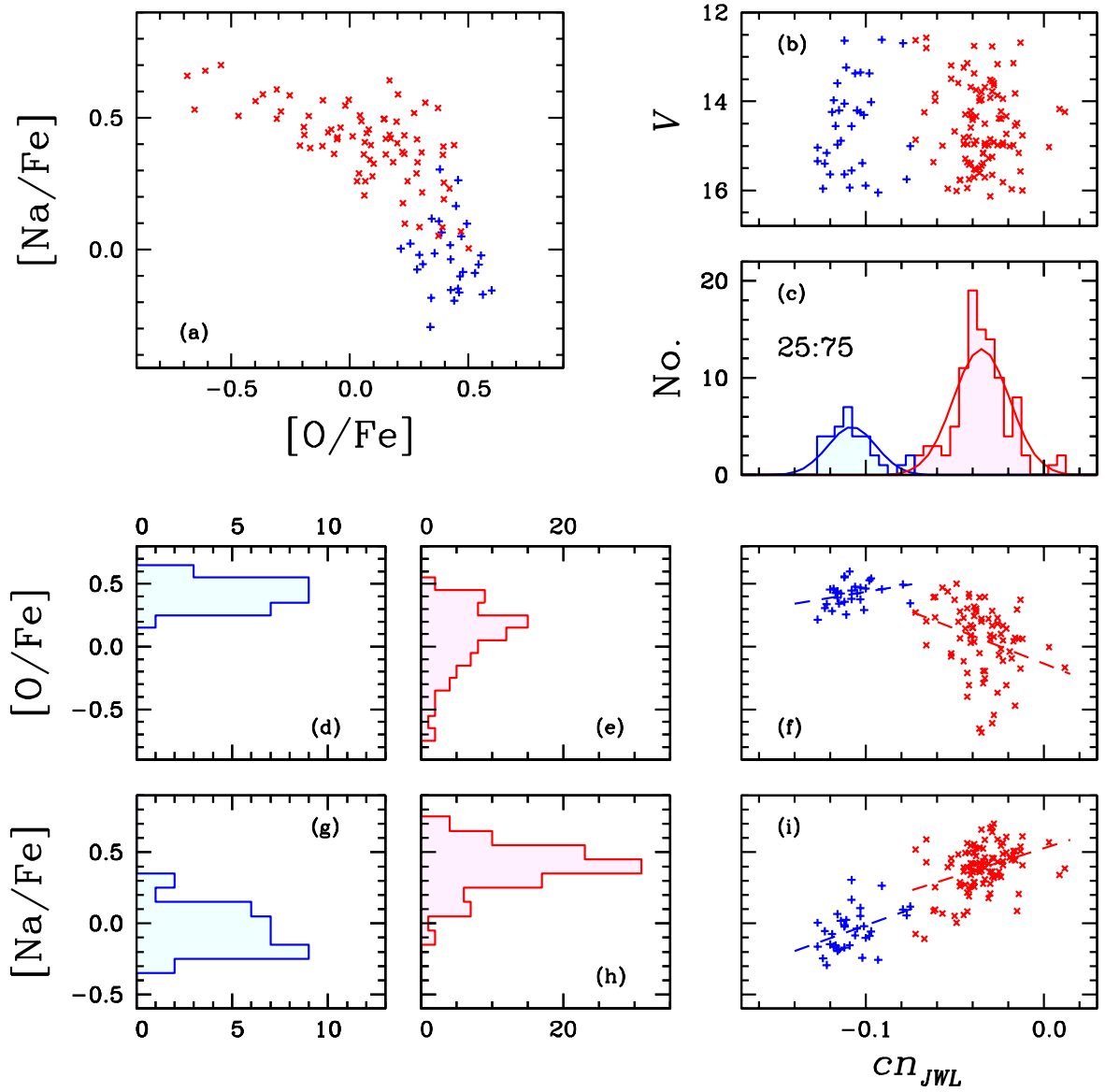


Fig. 9.— (a) The Na-O anticorrelation of M5 RGB stars by Carretta et al. (2009). The CN-w and CN-s stars based on the EM estimator are shown with blue plus signs and red crosses. (b) The cn_{JWL} versus V CMD of RGB stars studied by Carretta et al. (2009). (c) The cn_{JWL} distribution. (d)–(e) The $[\text{O}/\text{Fe}]$ distributions of the CN-w and the CN-s RGB stars. (f) A plot of cn_{JWL} versus $[\text{O}/\text{Fe}]$. Note that there appear to exist two separate cn_{JWL} - $[\text{O}/\text{Fe}]$ (anti)correlations. The cn_{JWL} - $[\text{O}/\text{Fe}]$ of the CN-w population is positively correlated, while that of the CN-s population is anticorrelated. (g)–(h) The $[\text{Na}/\text{Fe}]$ distributions of the CN-w and the CN-s RGB stars. (i) A plot of cn_{JWL} versus $[\text{Na}/\text{Fe}]$. The cn_{JWL} - $[\text{Na}/\text{Fe}]$ of both populations are positively correlated, albeit the correlations in the two populations may not be continuous.

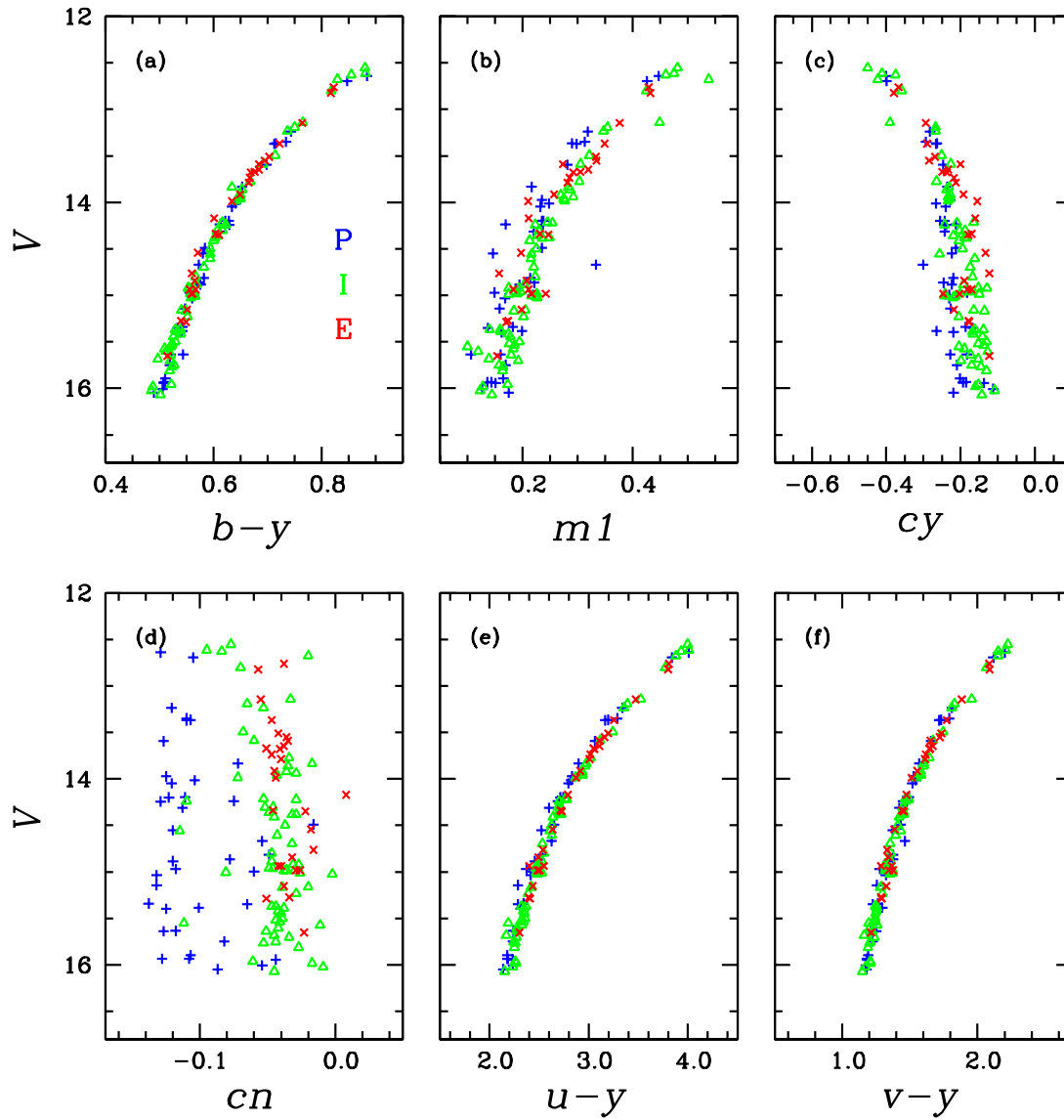


Fig. 10.— CMDs of spectroscopic target RGB stars of Carretta et al. (2009). The blue plus signs denote the primordial, the green open triangles the intermediate, and the red crosses the extreme populations defined by Carretta et al. (2009). From the photometric point of view, there is no difference between the intermediate and the extreme populations defined by Carretta et al. (2009).

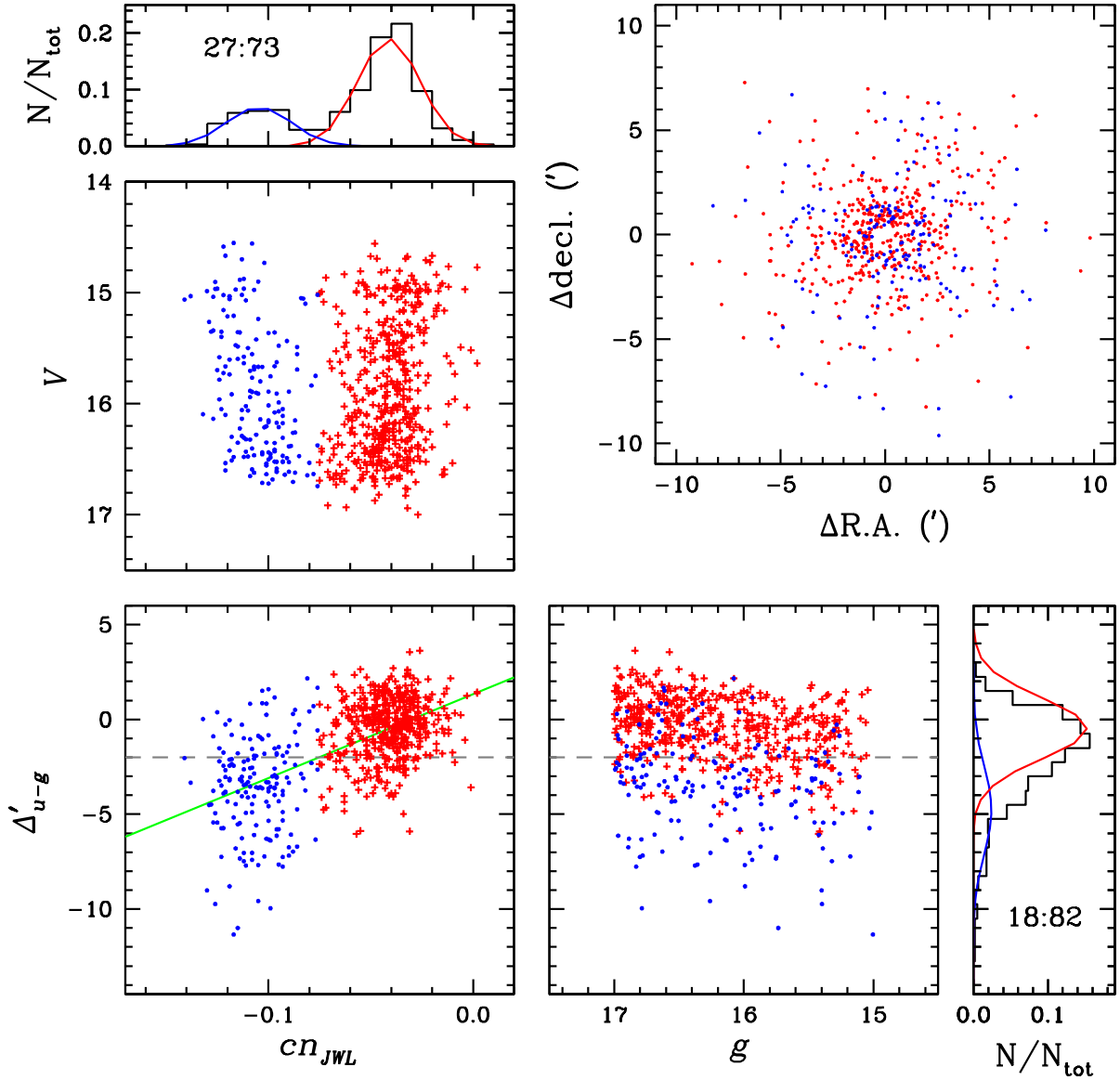


Fig. 11.— A comparison of our photometry with that of Lardo et al. (2011). The RGB stars with $\Delta'_{u-g} < -2$ are classified as the *UV-blue* and those with ≥ -2 as the *UV-red* stars by Lardo et al. (2011). The green solid line in the lower left panel represents the linear fit to the data. Our CMD shows bimodal RGB sequences, while that of Lardo et al. (2011) does not show clear separation between MSPs, suggesting that the boundary between the two populations set by Lardo et al. (2011) is rather arbitrary. Also note the continuous transition, with severe superpositions of the two populations, from the CN-w to the CN-s along the Δ'_{u-g} . Our result strongly suggests that the SDSS photometric system is not adequate to study the MSPs in GCs.

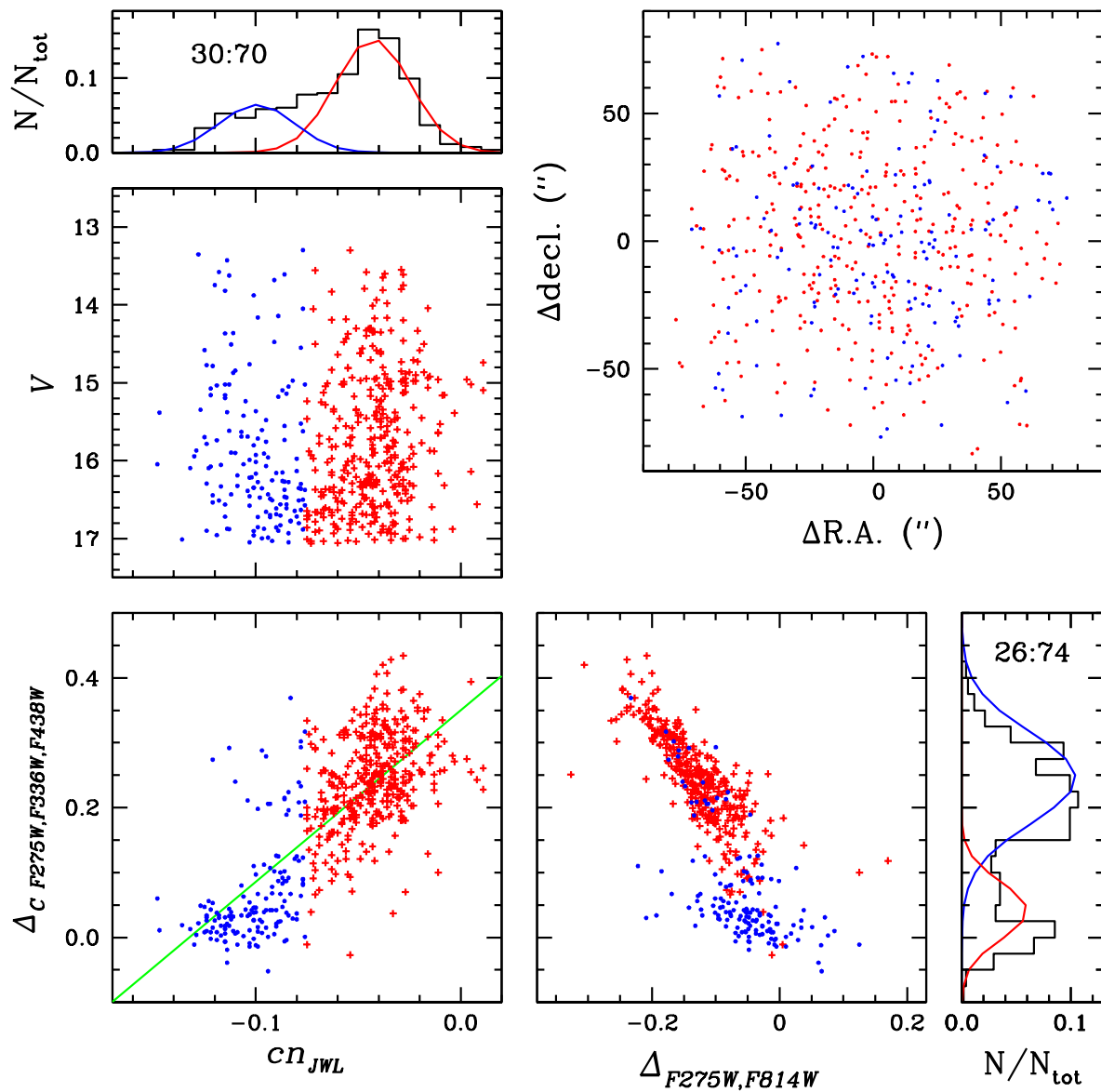


Fig. 12.— Same as Figure 11, but for Piotto et al. (2015). In general, our results are in good agreement with those of Piotto et al. (2015), although some confusion in the *HST* photometry can be seen.

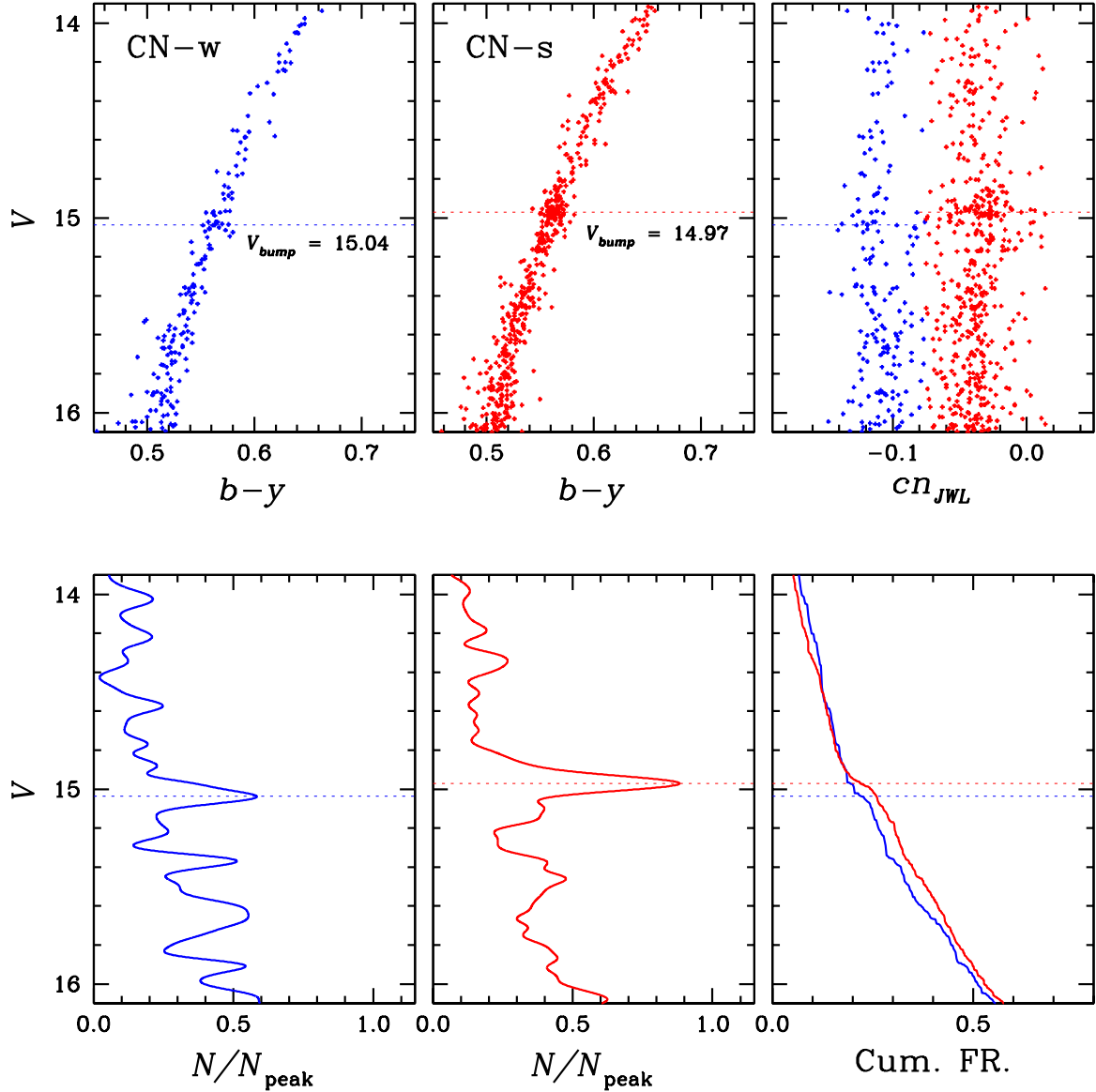


Fig. 13.— (Upper panels) Plots of $(b-y)$ versus V and cn_{JWL} versus V CMDs of the CN-w and the CN-s RGB stars in M5. The dashed lines are the V magnitude of the RGB bump, V_{bump} . We obtained $V_{\text{bump}} = 15.04$ mag for the CN-w population and 14.97 mag for the CN-s population. Note that the V_{bump} magnitudes of each population do not show any radial gradient (see Table 6). (Lower panels) Generalized histograms for RGB stars against V magnitude and the cumulative LFs for the CN-w and the CN-s populations. Although small, the V_{bump} of the CN-s population is slightly brighter, which may reflect the fact that the CN-s population has an enhanced helium abundance, $\Delta Y = 0.028$.

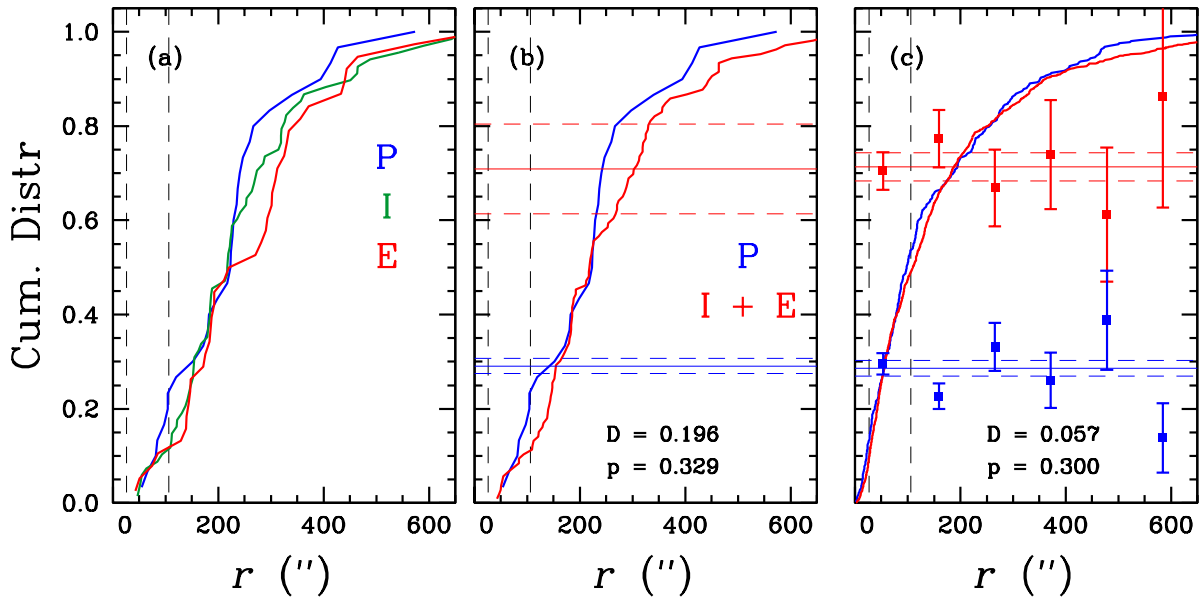


Fig. 14.— (a)–(b) The radial distributions of the multiple stellar populations based on the definition of individual populations by Carretta et al. (2009), showing that the primordial population appears to be more centrally concentrated than other populations. In (b) the blue and red horizontal lines are for the fraction of the primordial population, $n(\text{P})/n(\text{P}+\text{I}+\text{E}) = 0.291 \pm 0.016$, and the fraction of the intermediate and the extreme populations, $n(\text{I}+\text{E})/n(\text{P}+\text{I}+\text{E}) = 0.709 \pm 0.095$. The vertical black dashed lines are for the core and the half-light radii of the cluster. (c) The radial distributions of the CN-w (blue) and the CN-s (red) populations in M5. The blue and the red horizontal lines are for the fraction of the CN-w and the CN-s populations, $n(\text{CN-w})/n(\text{CN-w} + \text{CN-s}) = 0.286 \pm 0.017$ and $n(\text{CN-s})/n(\text{CN-w} + \text{CN-s}) = 0.714 \pm 0.030$. Our K-S test suggest that the radial distributions of the two populations are likely drawn from the identical parent distribution. Also note that the fractions of the CN-w and the CN-s populations do not appear to vary against the radial distance from the center.

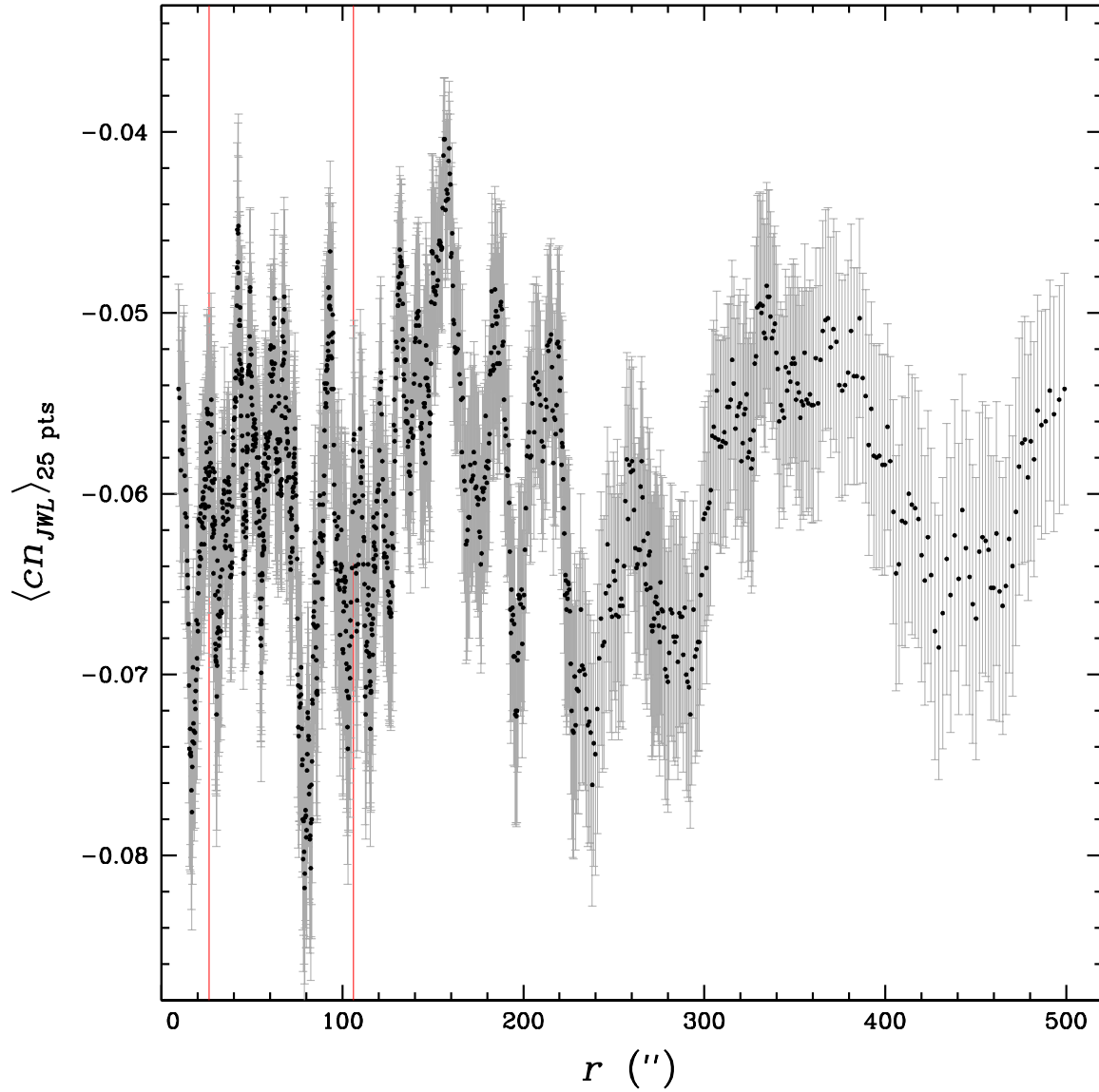


Fig. 15.— The moving average from the adjacent 25 points for our cn_{JWL} index of the RGB stars with $-2 \leq V - V_{HB} \leq 2$ mag against the radial distance from the center. The thin grey error bars represent the standard error of the mean and vertical thin red solid lines are for the core and the half-light radii of the cluster. The mean cn_{JWL} does not significantly vary against the radial distance, consistent with Figure 14(c).

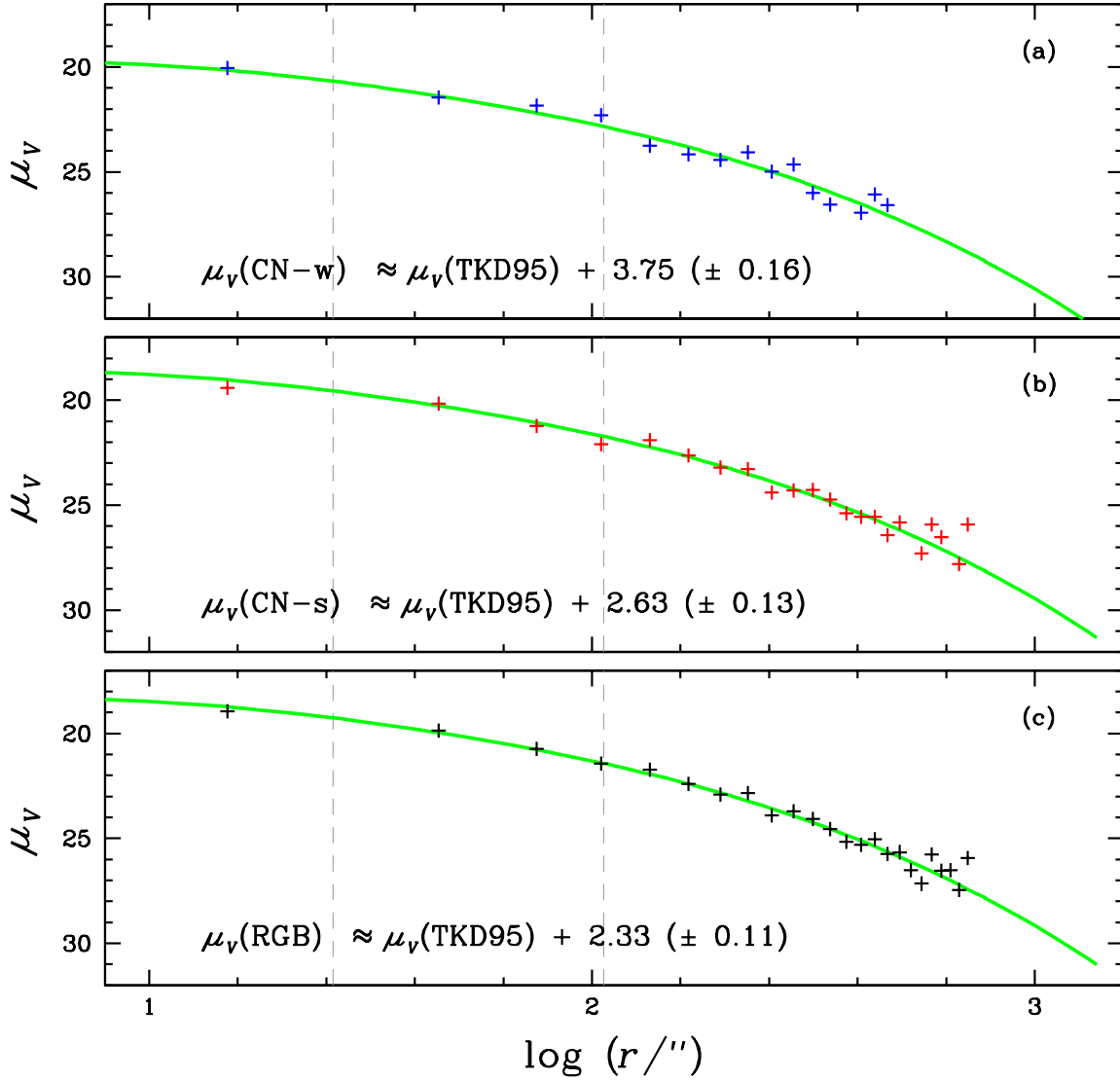


Fig. 16.— Surface-brightness profiles for the RGB stars with $-2 \leq V - V_{\text{HB}} \leq 2$ mag: (a) CN-w RGB stars only; (b) CN-s stars only; and (c) all RGB stars in M5. Green lines denote the Chebyshev polynomial fit of surface-brightness profile of M5 by Trager, King, & Djorgovski (1995). Our surface-brightness profiles for M5 are in excellent agreement with that of Trager, King, & Djorgovski up to $10'$ from the center of the cluster. The vertical grey dashed lines are for the core and the half-light radii of the cluster.

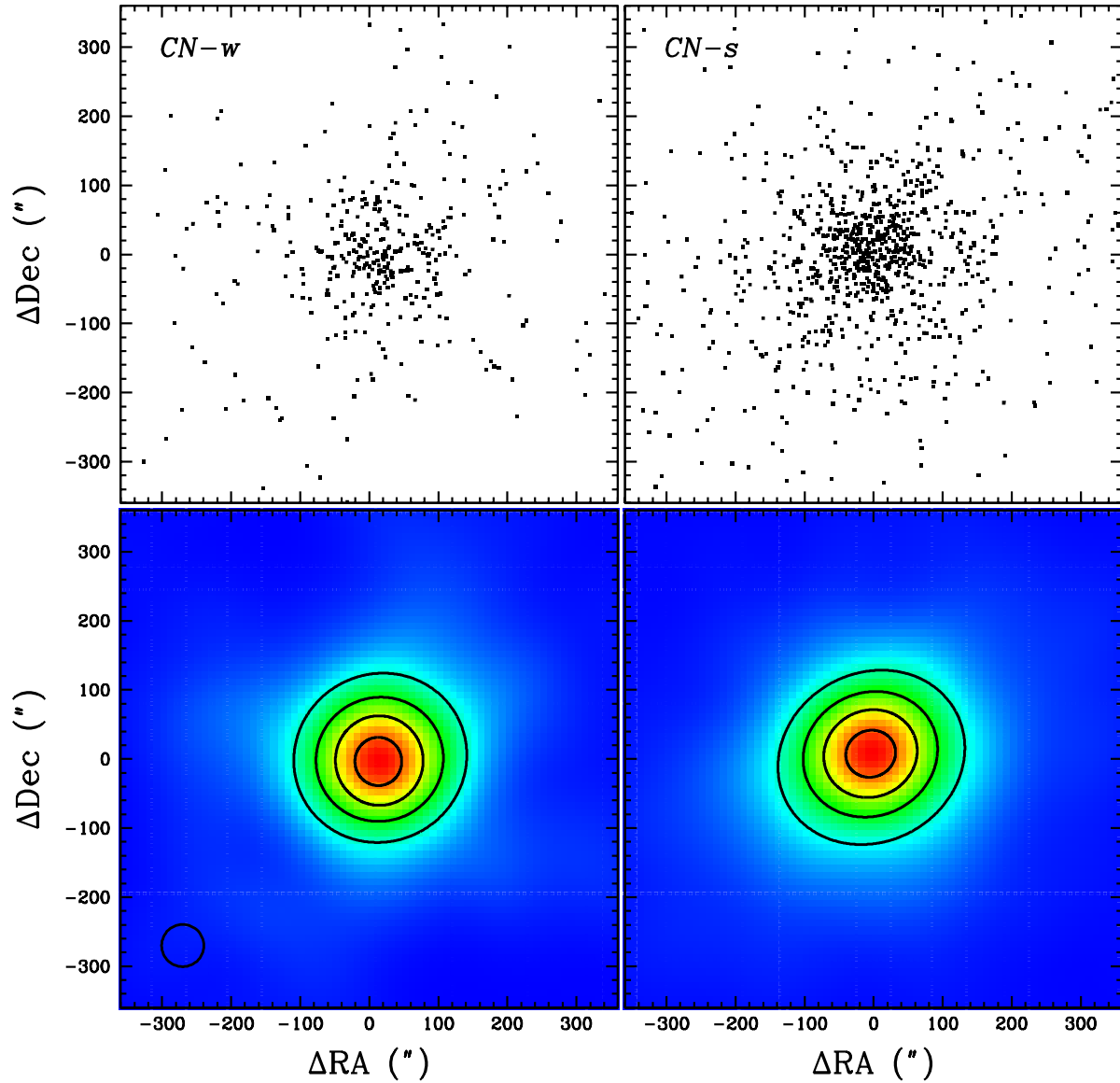


Fig. 17.— (Upper panels) Spatial distributions of the CN-w and the CN-s RGB stars in M5. (Lower panels) The smoothed contour maps using the fixed Gaussian kernel, where we show the iso-density contour lines for 90, 70, 50, and 30% of the peak values for both populations. We also show the FWHM of our adopted Gaussian kernel in the lower left panel of the figure. Note that the spatial distribution of the CN-s RGB population is more elongated along the NE-SW direction.

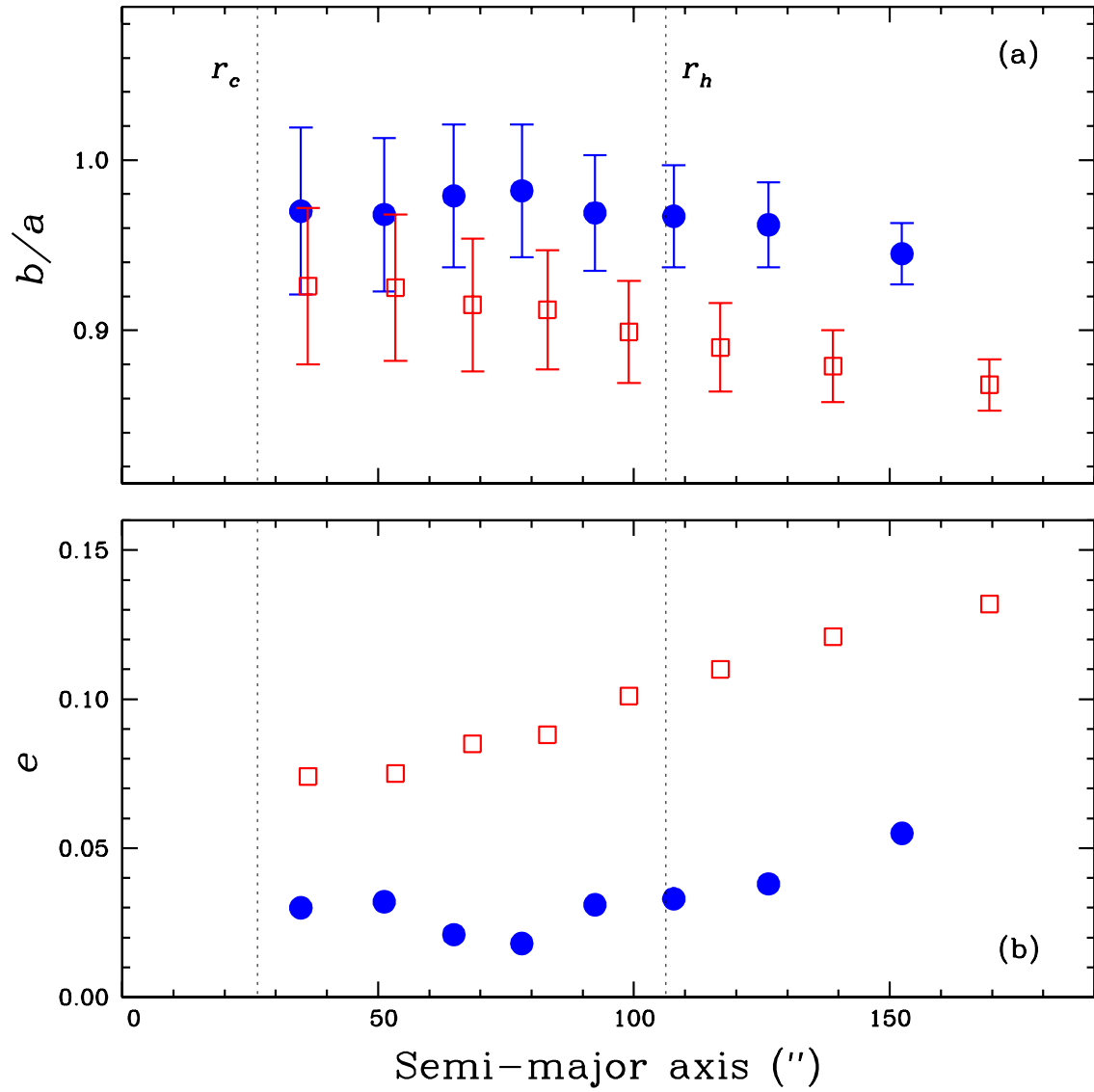


Fig. 18.— The run of the axial ratio, b/a , the ellipticity, $e (= 1 - b/a)$ of the CN-w (blue) and the CN-s (red) populations against the major axis, a . Note that the ellipticity of the CN-s population is significantly larger than that of the CN-w, consistent with our results shown in Figure 17.

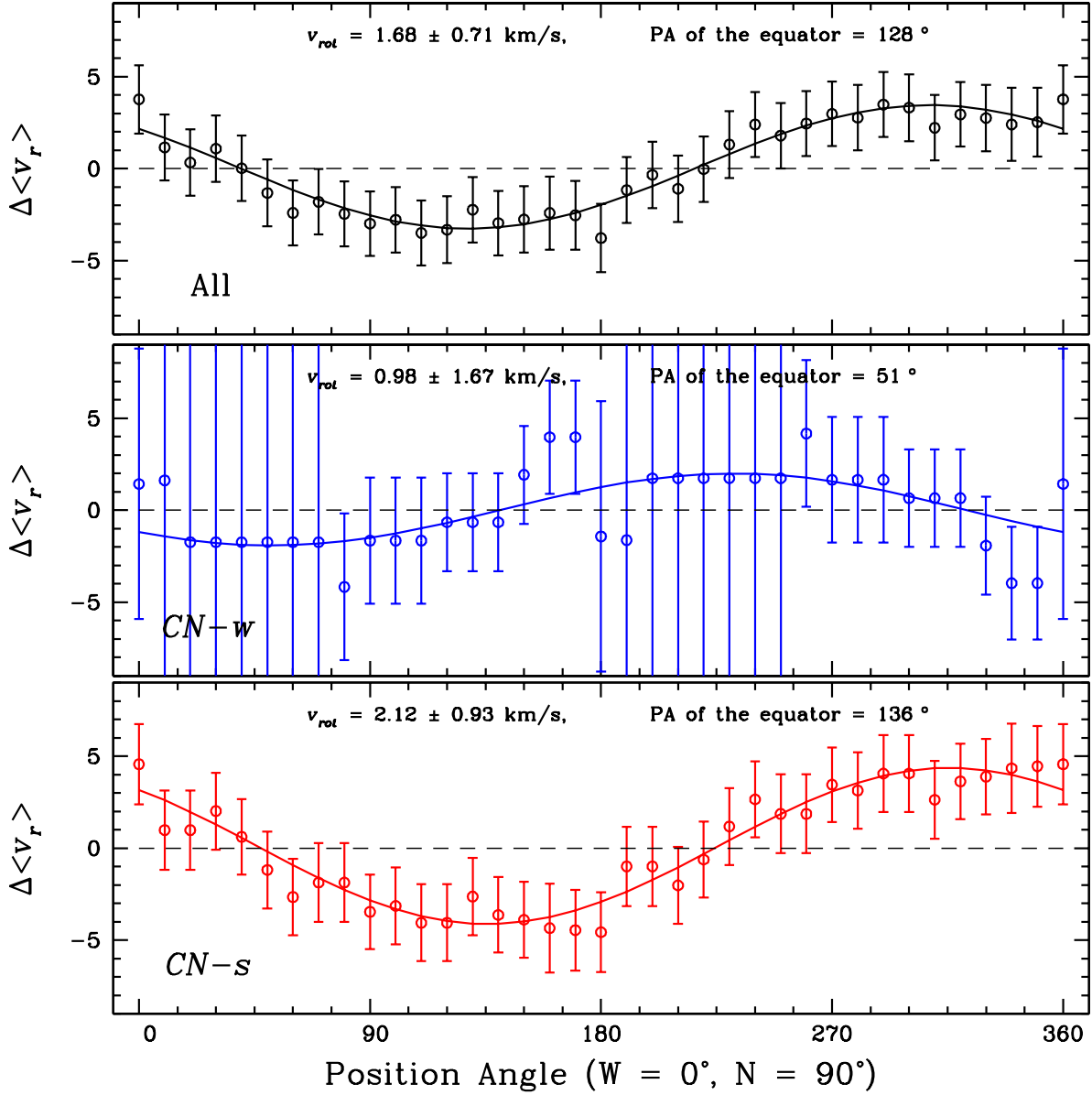


Fig. 19.— The difference in the mean radial velocities between both hemispheres against its position angle, where the net rotation is the half of the amplitude of the sinusoidal fit. It is evident that the CN-s population shows a substantial rotation, while the CN-w population does not. The position angle refers to that of the equator and the error bar is the error of the mean. The position angle of the equator of the projected rotation for the CN-s population, 136° (i.e., along the NE-SW direction), is consistent with the CN-s RGB distribution shown in Figure 17.

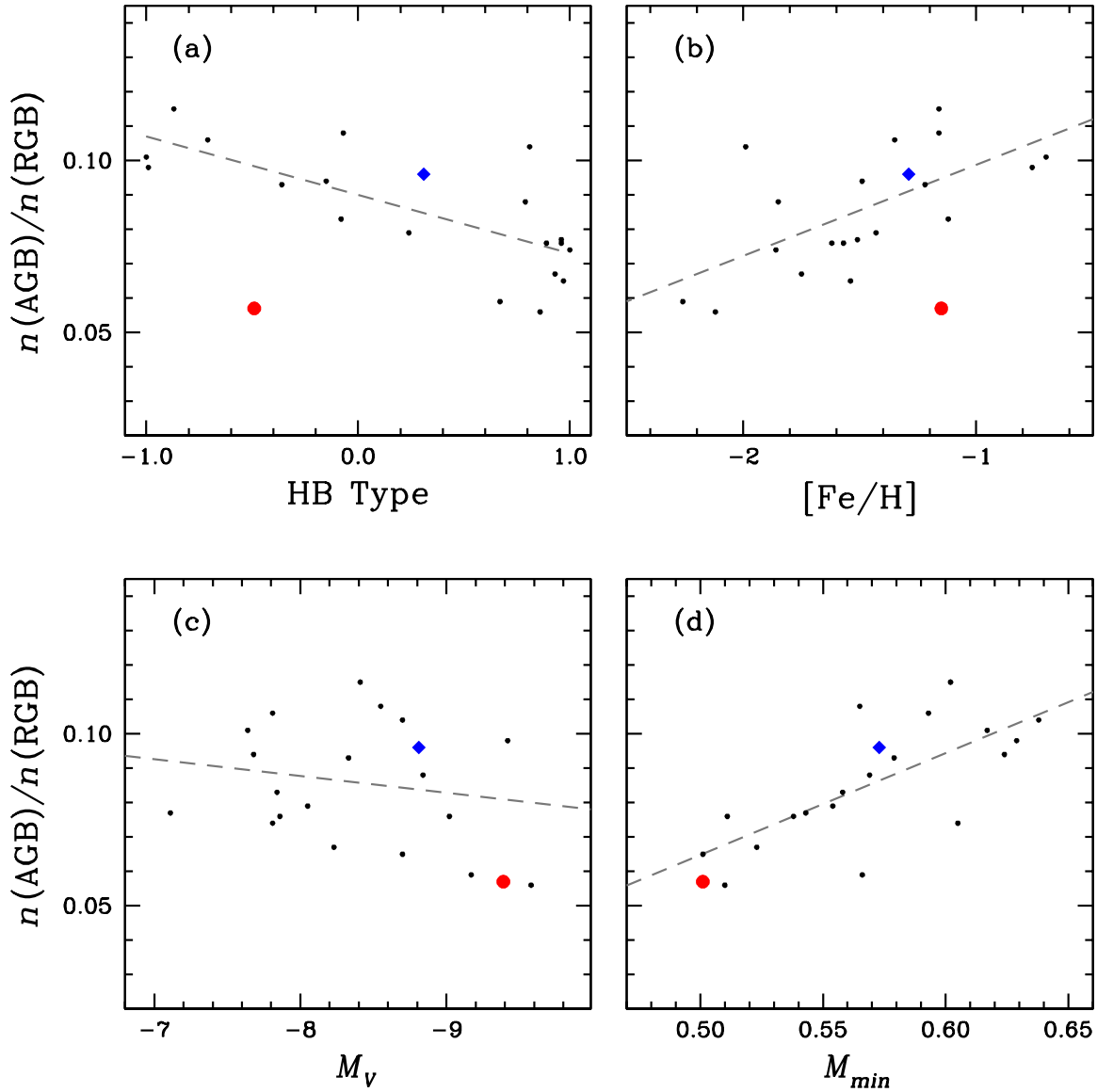


Fig. 20.— The relative AGB frequencies for GCs studied by Gratton et al. (2010). The blue diamonds and red circles denote M5 and NGC 2808, respectively. Note that M5 is located near the upper limit of the relative AGB frequency, indicating that the missing AGB population would be negligible for M5. The peculiar GC NGC 2808 appears to be an outlier and it is not included in deriving linear correlations in each panel.

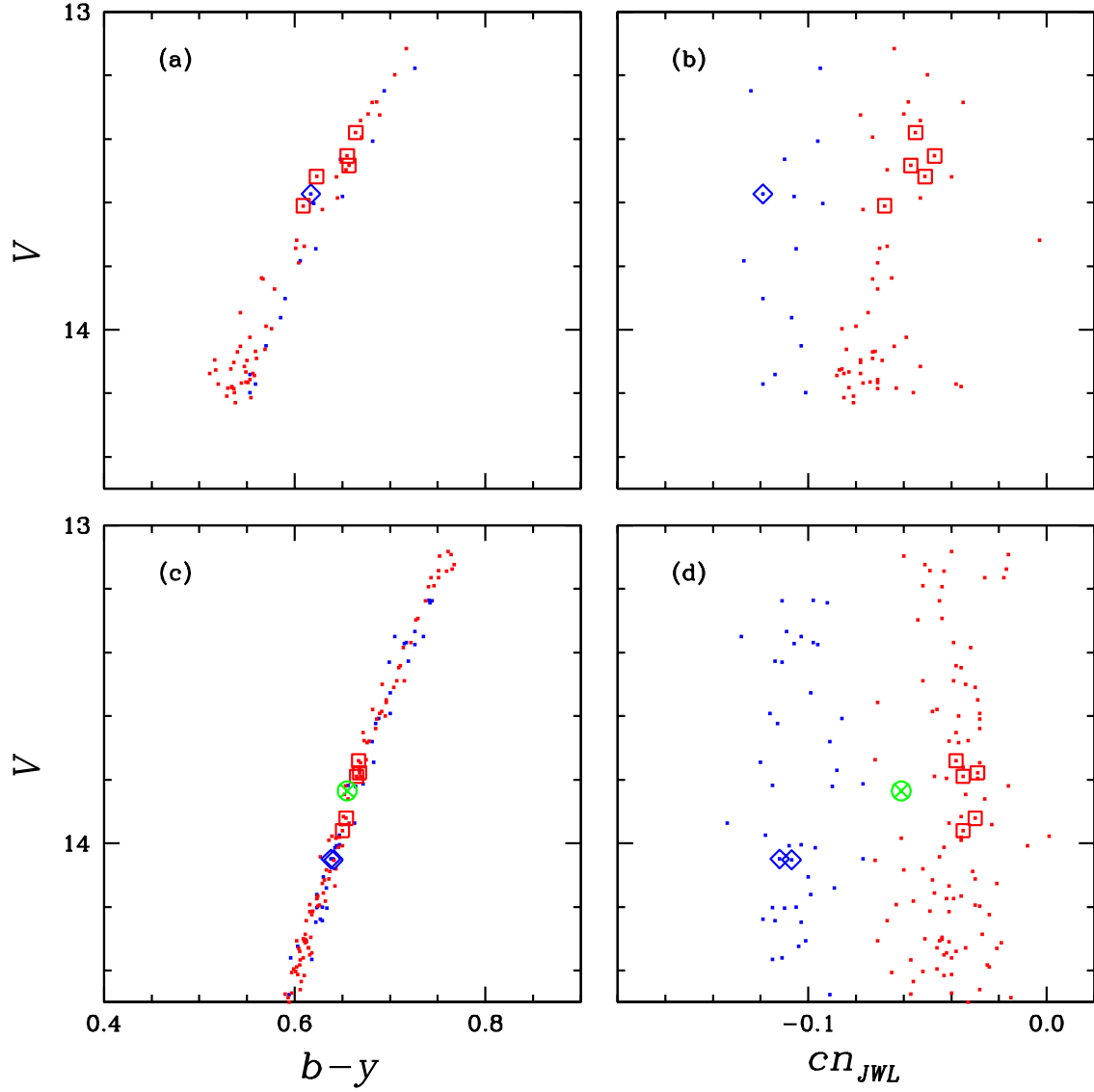


Fig. 21.— (a) The $(b - y)$ versus V CMD for M5 AGB stars. We also show AGB stars studied by Smith & Norris (1993). The blue open diamond is the CN-weak AGB star (IV-26) and the red open squares the CN-strong AGB stars by Smith & Norris (1993). (b) The cn_{JWL} versus V CMD for M5 AGB stars. Note the discrete double AGB sequences, as already shown in Figure 8. The blue dots are the CN-w and the red dots are the CN-s AGB stars based on the EM estimator, consistent with the classification made by Smith & Norris (1993). (c)–(d) Same as (a)–(b) but for RGB stars. The green open circle is for the CN-intermediate RGB star (II-50).

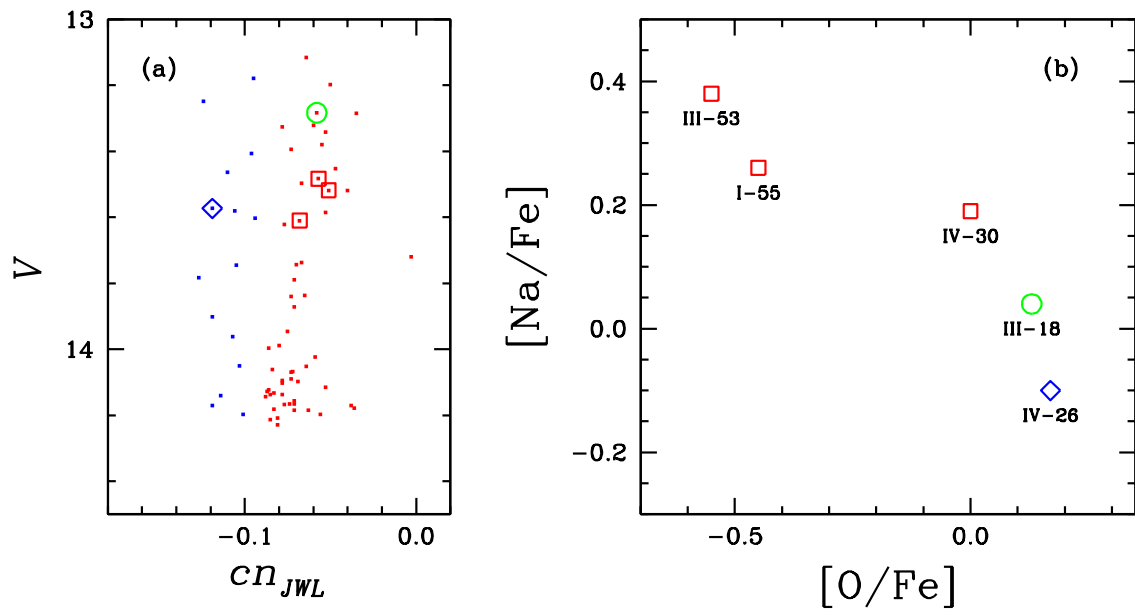


Fig. 22.— (a) Same as Figure 21(d), but for AGB stars studied by Ivans et al. (2001). (b) The Na-O anticorrelation of M5 AGB stars. The Na-O anticorrelation is closely related with the double AGB sequences in M5, similar that can be seen in the RGB sequence.

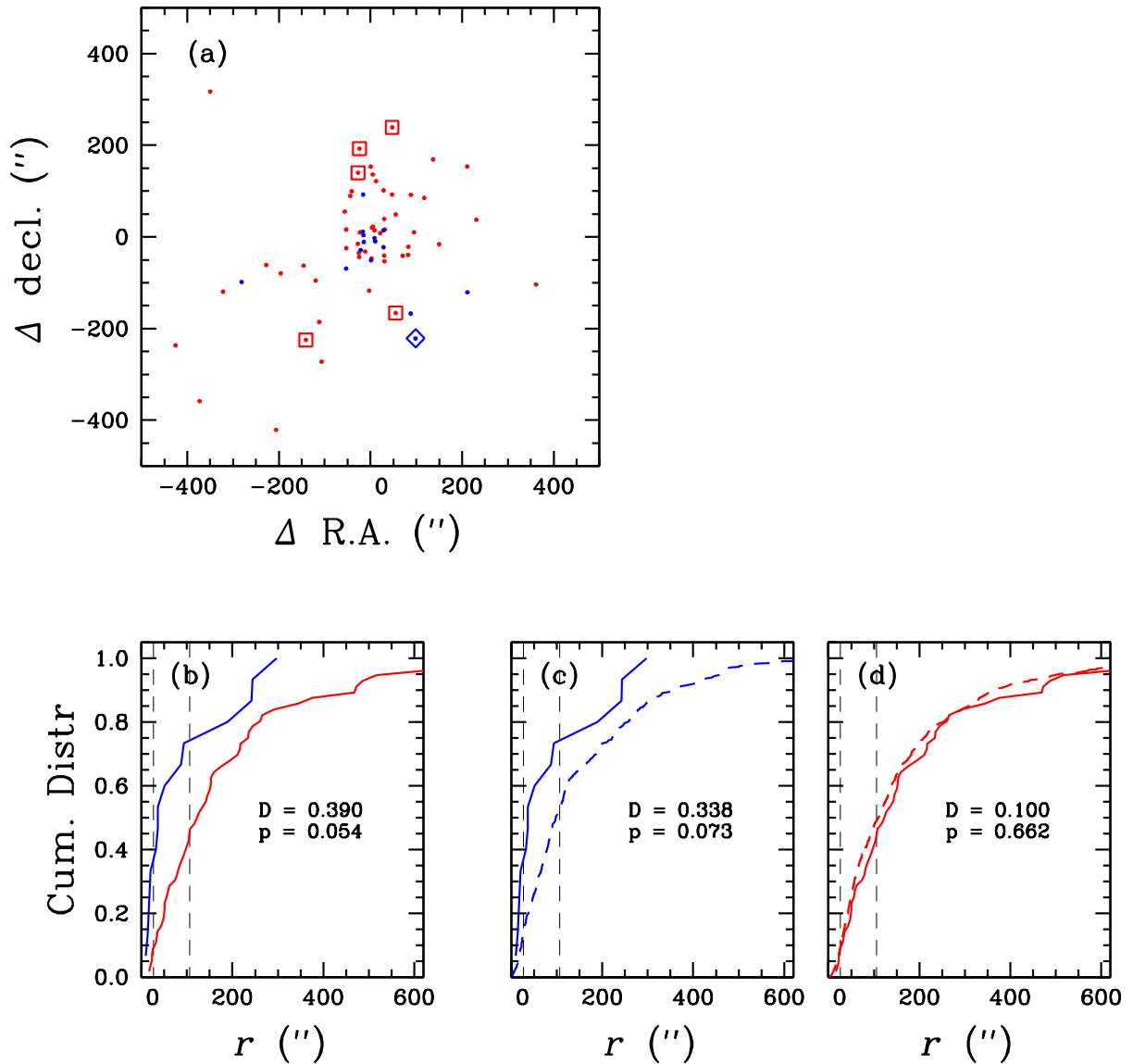


Fig. 23.— (a) The spatial distributions of the CN-w (blue dots) and the CN-s (red dots) AGB stars in M5. The blue open diamond and the red open squares are those studied by Smith & Norris (1993). Note that the distribution of the CN-s AGB stars is more elongated, stretched from NW to SE, similar to that of the CN-s RGB stars. (b) The radial distribution of the M5 AGB stars. The blue solid line denotes the CN-w AGB stars and the red solid line the CN-s AGB stars. The CN-w AGB stars are more centrally concentrated than the CN-s AGB stars are. The K-S test indicates that they are likely drawn from the different parent distributions. (c) A comparison of the radial distribution of the CN-w RGB (the dashed line) and the CN-w AGB (the solid line) stars. The two groups of stars are likely drawn from the different parent populations. (d) A comparison of the radial distribution of the CN-s RGB (the dashed line) and the CN-s AGB (the solid line) stars. The two groups of stars are most likely drawn from the same parent population.

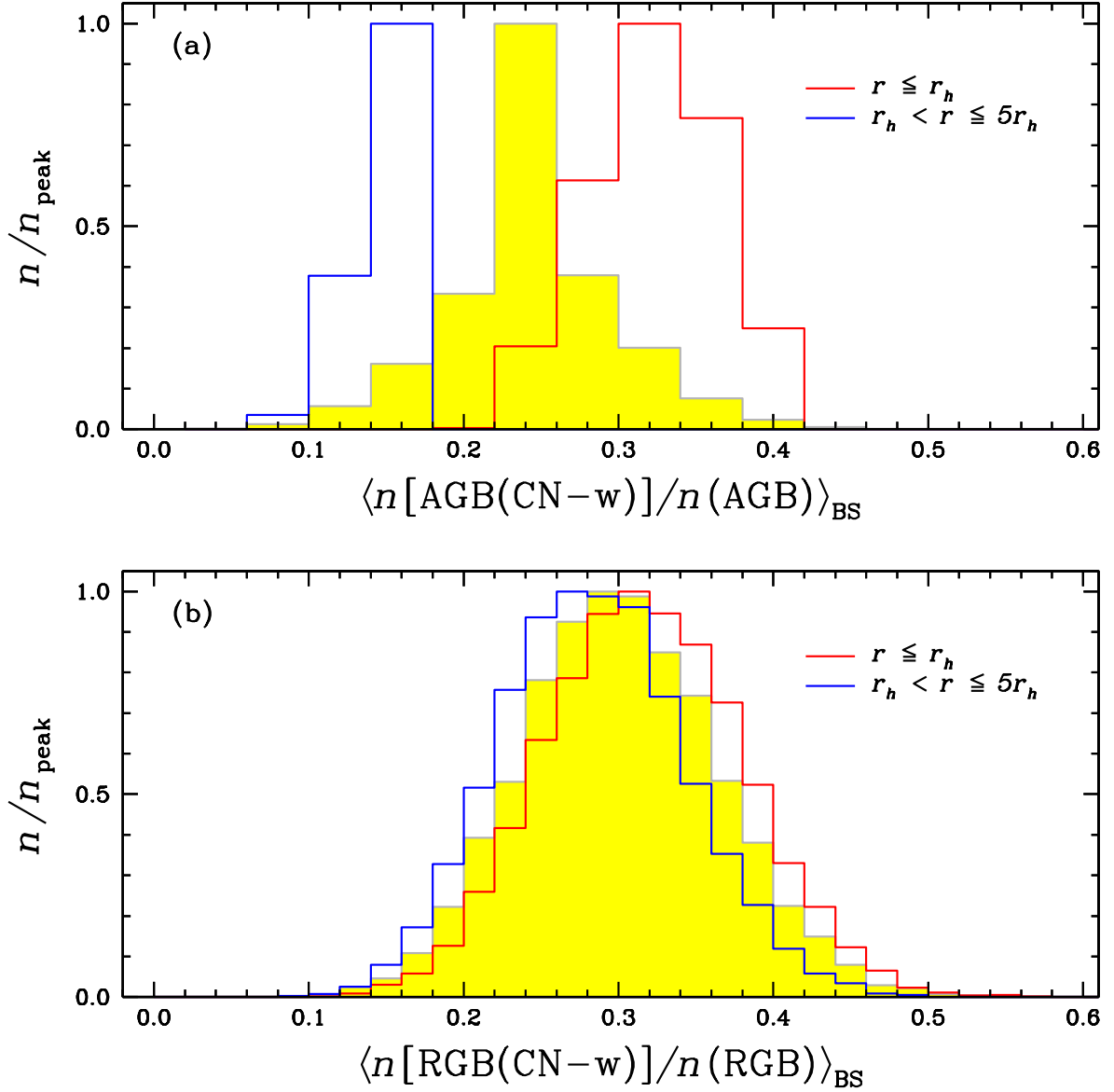


Fig. 24.— Empirical distributions of the mean value of relative fraction of the CN-w populations in the AGB (upper panel) and the RGB (lower panel) sequences from the bootstrap method. The red solid lines are for the inner region ($r \leq r_h$) and the blue solid lines are for the outer region ($r_h < r \leq 5r_h$) of the cluster. The yellow shaded histograms are for all stars within $5r_h$ from the center. Note that the mean frequency of the CN-w AGB population in the outer part of the cluster is significantly smaller than that in the inner part, most likely due to the stochastic truncation of the CN-w AGB stars in the outer part of the cluster.

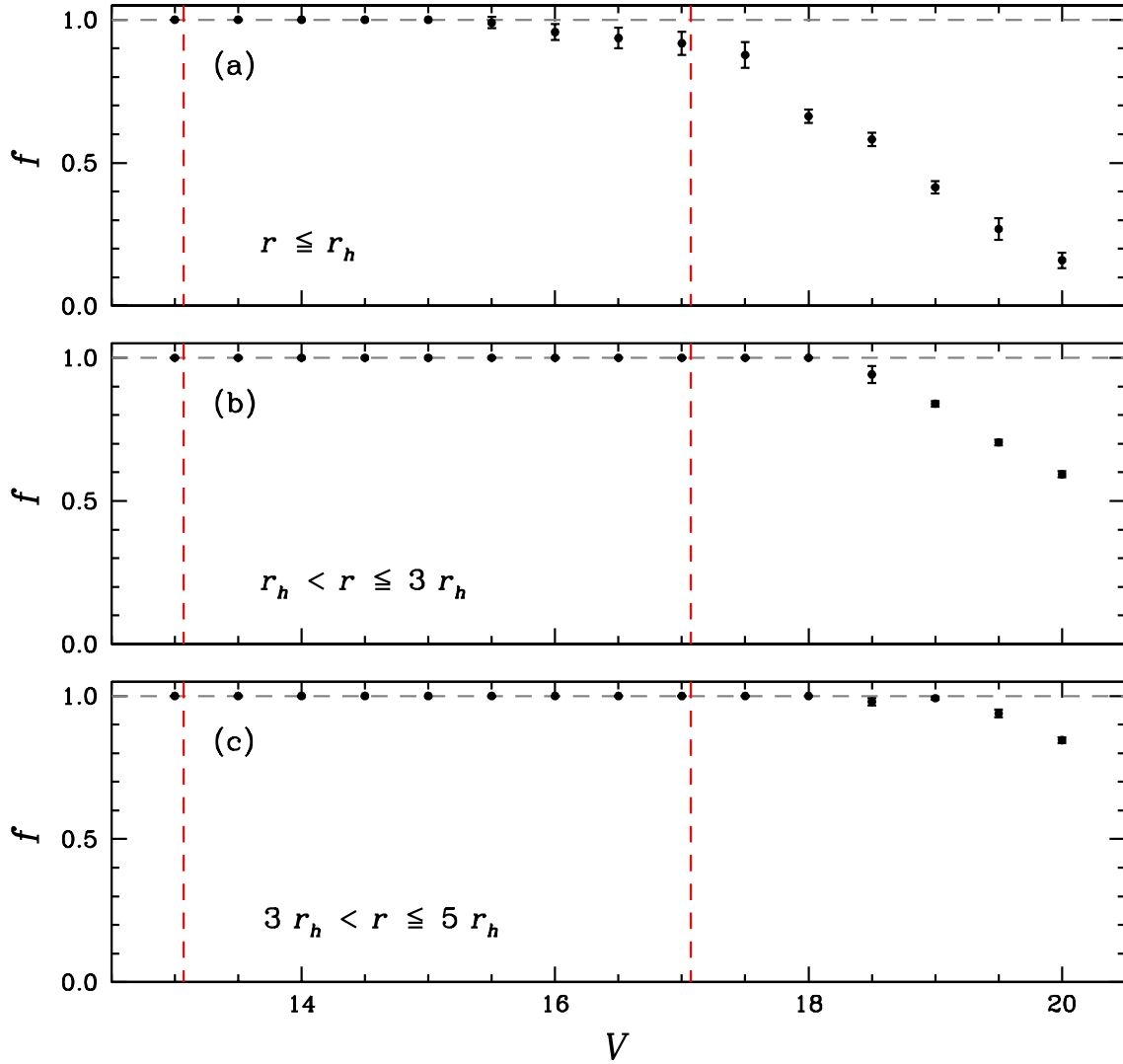


Fig. 25.— Completeness fractions at each magnitude bins measured from artificial star experiments for the inner, intermediate and outer regions of M5. The vertical dashed lines denote $V - V_{\text{HB}} = \pm 2.0$ mag, with $V_{\text{HB}} = 15.07$ mag for M5. Our experiments suggest that our photometry is complete down to $V = 18.0$ and 19.0 mag for the intermediate and the outer regions of M5, respectively. On the other hand, owing to the rather large apparent central crowdedness of M5, our photometry for the inner part of the cluster becomes incomplete at $V \approx 16.0$ mag, which is equivalent to $V - V_{\text{HB}} \approx 1.0$ mag.

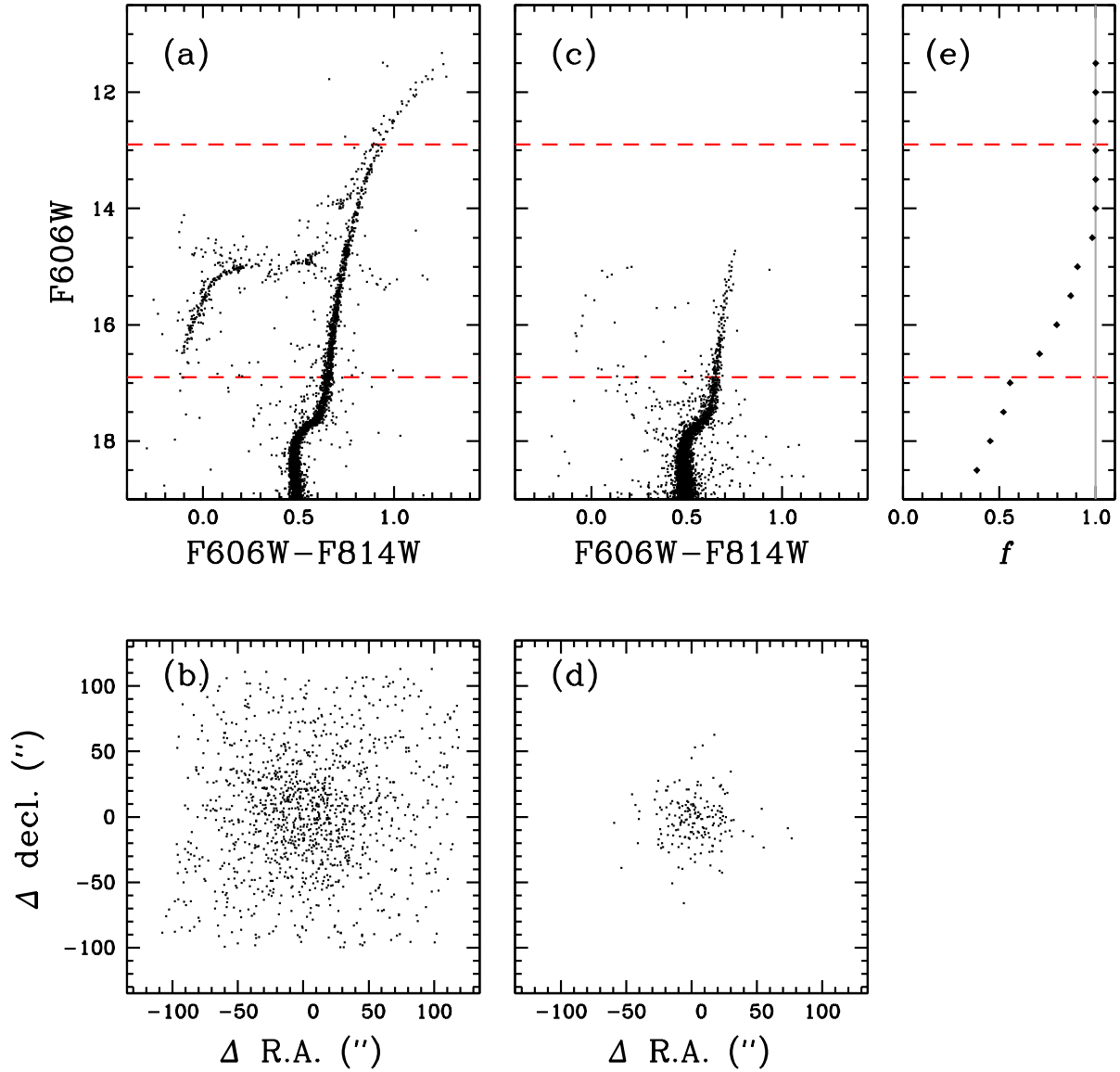


Fig. 26.— (a) The M5 *HST ACS* CMD (Anderson et al. 2008) using stars detected in our ground-based photometry. The horizontal red dashed lines denote $F606W - F606W_{HB} = \pm 2.0$ mag with $F606W_{HB} = 14.90$ (Dotter et al. 2010). (b) Positions of stars in (a) with $-2 \leq F606W - F606W_{HB} \leq +2$ mag. (c) The M5 *HST ACS* CMD using stars not detected in our ground-based photometry. (d) Positions of stars in (c) with $-2 \leq F606W - F606W_{HB} \leq +2$ mag. (e) Completeness fractions at each magnitude bins measured from the number of stars not detected in our ground-based photometry.

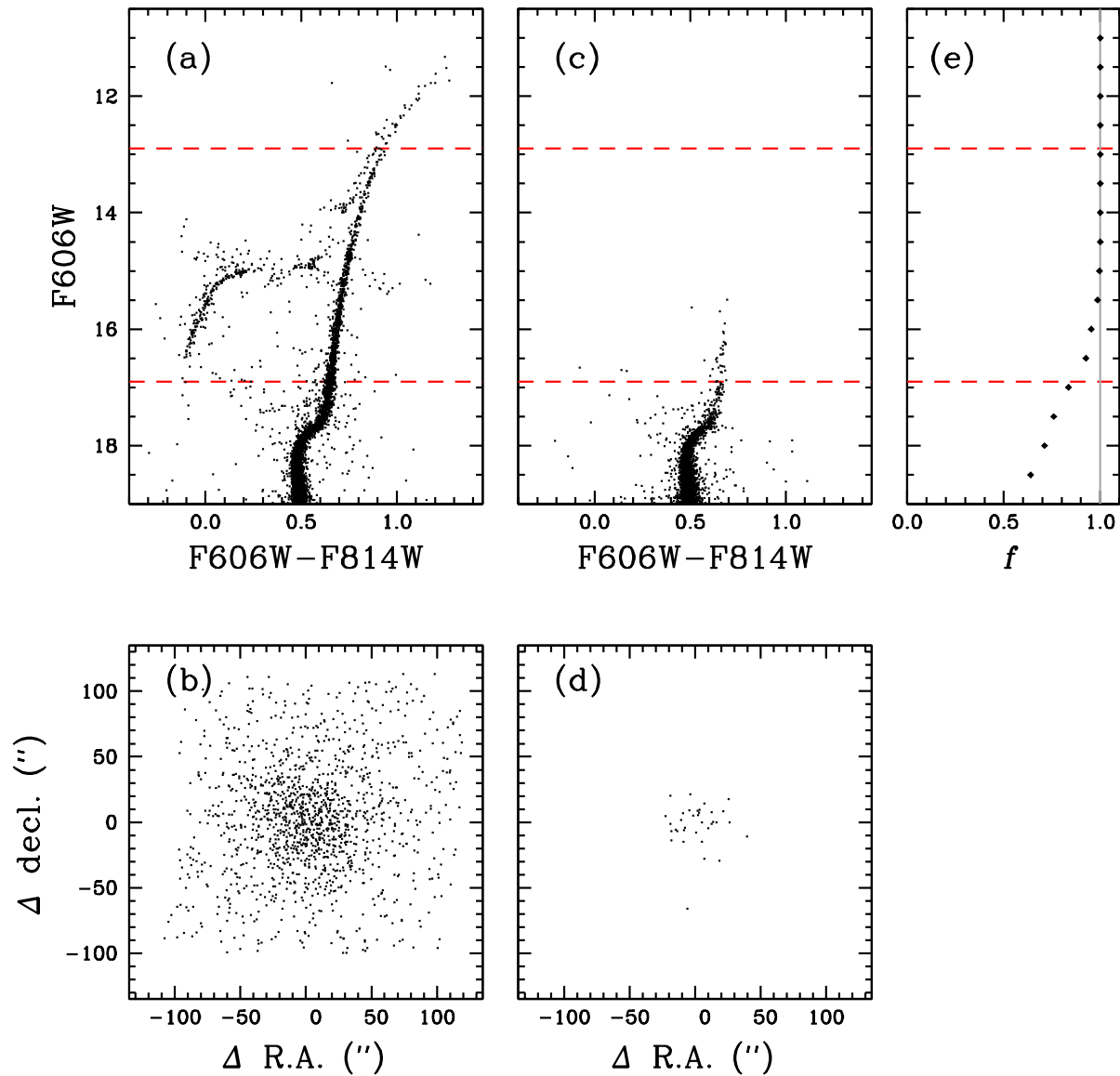


Fig. 27.— Same as Figure 26, but using our new ground-based photometry making use of the positions of the stars of the *HST ACS* photometry by Anderson et al. (2008). Note that our approach can significantly improve the detection rate in the central part of the cluster. Due to the unavoidable seeing effect in any ground-based observations, our photometry is still incomplete at the magnitude of our interest, $-2 \leq V - V_{\text{HB}} \leq 2.0$ mag. However, incomplete detection of stars in the central part of the cluster does not affect our results presented in this work.

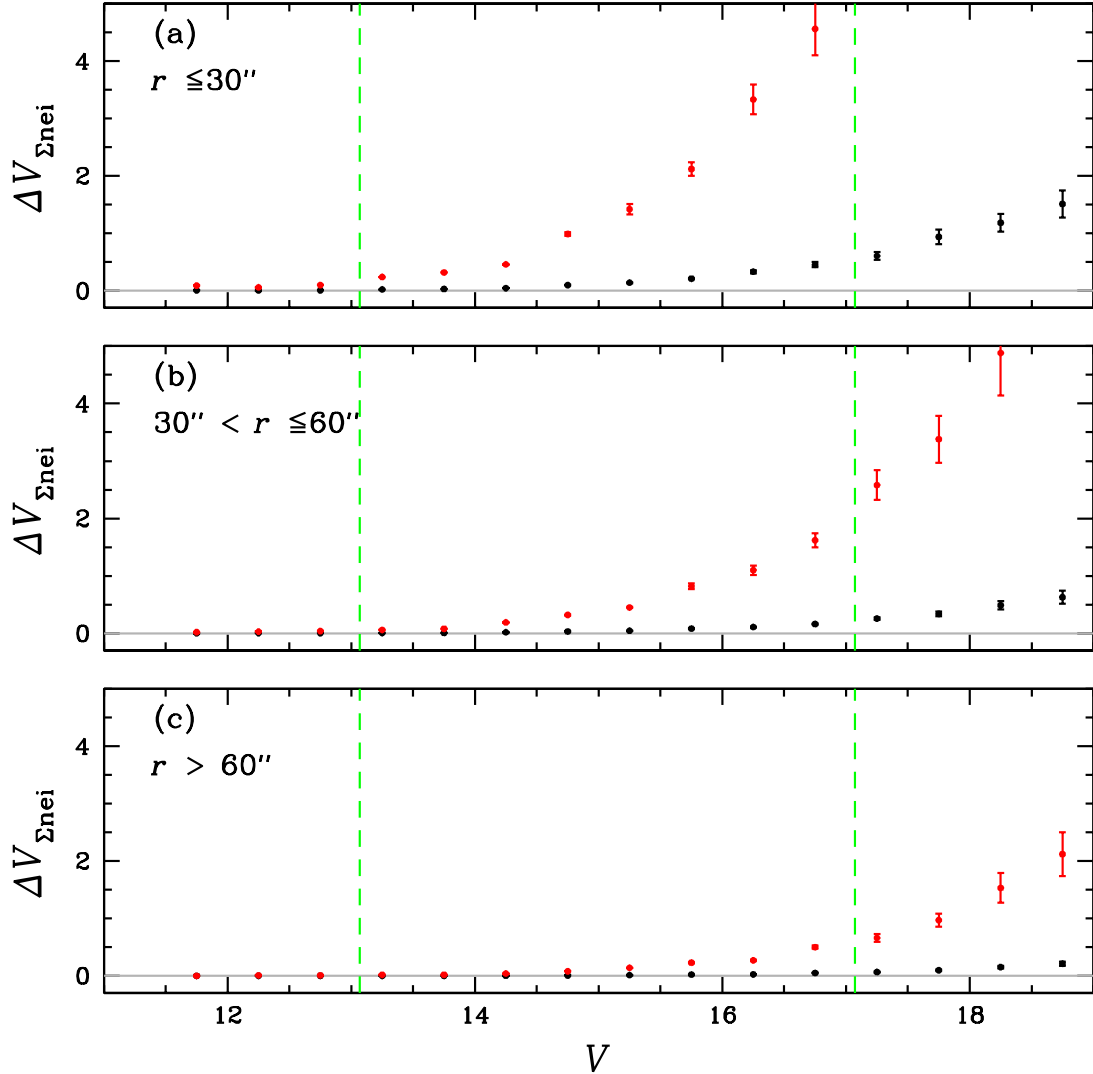


Fig. 28.— Estimation of the influence of the undetected nearby stars on the ground-based photometry. The black dots and error bars denote the mean magnitudes with $\pm 1\sigma$ of the sum of the surface brightness produced by nearby undetected stars in the ground-based observations. The red dots and error bars are for those ten times of black ones. The vertical green dashed lines denote $V - V_{HB} = \pm 2.0$ mag. In the inner part of M5 ($r \leq 1'$), the residual flux from the undetected nearby stars supplemented from the *HST ACS* photometry could cause the excess in the V magnitude of ≈ 0.08 mag at V_{HB} in our ground-based photometry. In practice, the undetected nearby stars do not appear to greatly affect the magnitude measurements as we already showed in Table 6. Instead, they increase the background brightness level of the central part and their net effect on the photometric measurements is almost nil if a sky background subtraction is properly applied.

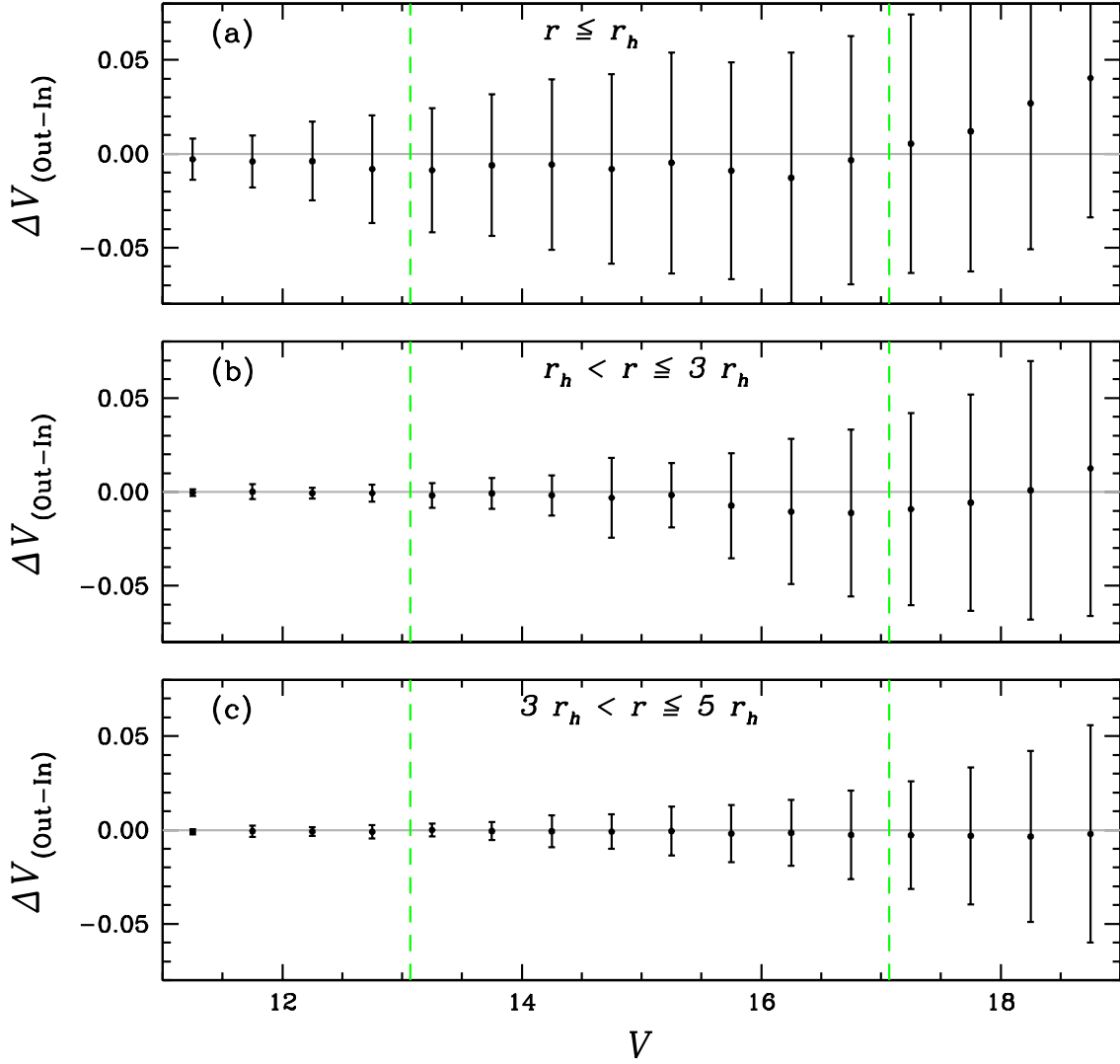


Fig. 29.— Comparisons of the input magnitudes to the output magnitudes from our artificial star experiments. The black dots and error bars denote the mean magnitudes with $\pm 1\sigma$ of the difference in magnitude. The vertical green dashed lines denote $V - V_{\text{HB}} = \pm 2.0$ mag. Our experiments show that the differences between the input and output magnitudes are spatially independent at the magnitude of our interest, $-2 \leq V - V_{\text{HB}} \leq 2.0$ mag, although the standard deviations of the mean in the inner part of M5 ($r \leq 1'$) are larger than those in the outer part.